AGU Advances

First Revision of

Subantarctic Mode Water Biogeochemical Formation Properties and Interannual Variability

Seth M. Bushinsky and Ivana Cerovečki

[1] Department of Oceanography, School of Ocean and Earth Science and Technology, University of Hawai'i at Mānoa, Honolulu, HI

[2] Scripps Institution of Oceanography, University of California San Diego, La Jolla, CA

Subantarctic Mode Water Biogeochemical Formation Properties and Interannual Variability

Seth M. Bushinsky[1] and Ivana Cerovečki[2]

[1]Department of Oceanography, School of Ocean and Earth Science and Technology, University of Hawai‘i at Mānoa, Honolulu, HI

[2]Scripps Institution of Oceanography, University of California San Diego, La Jolla, CA

Corresponding author: Seth Bushinsky (seth.bushinsky@hawaii.edu)

Key Points:

- Subantarctic Mode Water (SAMW) biogeochemical formation properties are a function of the density of newly formed water
- Newly formed SAMW is undersaturated in oxygen due to opposing effects from cooling (solubility) and entrainment, and air-sea injection
- SAMW is near or above atmospheric pCO_2 during formation and therefore not a strong direct sink of contemporary carbon dioxide

Abstract

Subantarctic Mode Water (SAMW) is a key water mass for the transport of nutrients, oxygen, and anthropogenic carbon into the ocean interior. However, a lack of biogeochemical observations of SAMW properties during wintertime formation precluded their detailed characterization. Here we characterize for the first time SAMW properties across their entire wintertime formation regions based primarily on biogeochemical profiling floats. Observations show that the SAMW properties differ between the two main formation regions in the Pacific and Indian sectors of the Southern Ocean. SAMW formed in the Pacific is colder, fresher, and higher in oxygen, nitrate, and dissolved inorganic carbon than its Indian Ocean counterpart. The relationship between potential density and biogeochemical water properties is nearly identical between the two formation regions; property differences thus predominantly reflect the difference in mean densities of SAMW formed in each region. SAMW is undersaturated in oxygen during formation, which will impact calculations of derived quantities that assume preformed oxygen saturation. SAMW is at or above atmospheric pCO_2 during wintertime and therefore not a direct sink of contemporary carbon dioxide during the formation period. Results from the Biogeochemical Southern Ocean State Estimate suggest anti-correlated interannual variability in dissolved inorganic carbon, nitrate, and oxygen in the central and southeastern Pacific formation regions similar to previously established patterns in mixed layer physical properties. This indicates that the mean properties of SAMW will vary depending on which sub-region has a stronger formation rate, which is in turn linked to the Southern Annual Mode and the El-Niño Southern Oscillation.

Plain Language Summary

In the Southern Ocean, north of the Antarctic Circumpolar Current, wintertime surface ocean heat loss cools the water, increasing its density and forming thick layers of well mixed water that enter the ocean. This water, called Subantarctic Mode Water (SAMW), represents an important pathway for anthropogenic carbon, nutrients and oxygen into the ocean interior. In this study we used new wintertime observations from profiling robots equipped with sensors that measure oxygen, nitrate, and pH in the top 2000 m to determine important initial properties of SAMW for the first time. We find that the SAMW properties differ between the Pacific and Indian formation regions and are related to the densities of SAMW formed in each basin. These properties indicate that it is unlikely for SAMW to take up present-day carbon dioxide from the atmosphere during formation,

53 though it may still absorb anthropogenic carbon. We investigated how these properties varied year-
54 to-year using an ocean model linked to observations, finding connections between changes in the
55 biogeochemical properties and physical processes as well as large-scale climate variability. These
56 results will provide valuable constraints on interpretation of subsurface ocean measurements and
57 model studies investigating the role of these waters in the global carbon cycle.
58
59
60

1. Introduction

The Southern Ocean is responsible for 50% of the contemporary carbon absorbed by the ocean each year (DeVries 2014; Le Quéré et al. 2018; Friedlingstein et al. 2019). This contemporary carbon uptake by the Southern Ocean is largely driven by a strong anthropogenic carbon flux overlaid on a balanced natural carbon cycle (Gruber et al. 2019b). North of the Antarctic Circumpolar Current (ACC), the uptake of natural carbon is driven by Thermocline Waters (TW) from the subtropics that cool as they are advected south and are the site of biological production, both of which lower the partial pressure of CO_2 (pCO_2) in the ocean, drawing down carbon from the atmosphere (Mikaloff Fletcher et al. 2007; Gruber et al. 2009b, 2019b). This uptake is balanced by the upwelling of Circumpolar Deep Water (CDW) enriched in old carbon from degraded biological material that is released to the atmosphere as CDW waters reach the surface south of the ACC. A fraction of the upwelled CDW is advected southward, where it cools and subducts as Antarctic Bottom Water, while another fraction is advected northward, mixing with TWs advected southward, forming mode and intermediate waters (Iudicone et al. 2011; Morrison et al. 2015). Newly formed Subantarctic Mode Water (SAMW) contains a mix of CDW, Antarctic Intermediate Water (AAIW), older SAMW that is re-entrained as intense surface heat loss during the winter drives deep winter mixed layers and subduction, and TW (McCartney 1977; Hanawa and Talley 2001). After subduction, these well-mixed, near-surface layers are advected away from their formation regions into the ocean interior (McCartney 1977, 1982). SAMW primarily forms in the Indian and Pacific sectors of the Southern Ocean, where wintertime mixed layers are deepest (Figure 1).

After subduction, SAMW is advected by the ACC and can either be re-entrained and modified during subsequent winter mixed layer (ML) deepening or exported into the ocean interior where it is advected by the subtropical gyre circulation (Hanawa and Talley 2001; Koch-Larrouy et al. 2010; Hartin et al. 2011; Cerovečki et al. 2019; Morrison et al. 2022). SAMW redistributes heat and freshwater from the Southern Ocean to the tropics (Wong et al. 1999) and the export of nutrients from the Southern Ocean through mode and intermediate waters fuels between 44 and 75% of global ocean productivity (Sarmiento et al. 2004; Primeau et al. 2013). SAMW is also one of the major water masses that transports anthropogenic and natural carbon into the ocean interior from the Southern Ocean, based on interior measurements of dissolved inorganic carbon (DIC) and modeling inversion studies (Mikaloff Fletcher et al. 2006, 2007; Gruber et al. 2009b, 2019b).

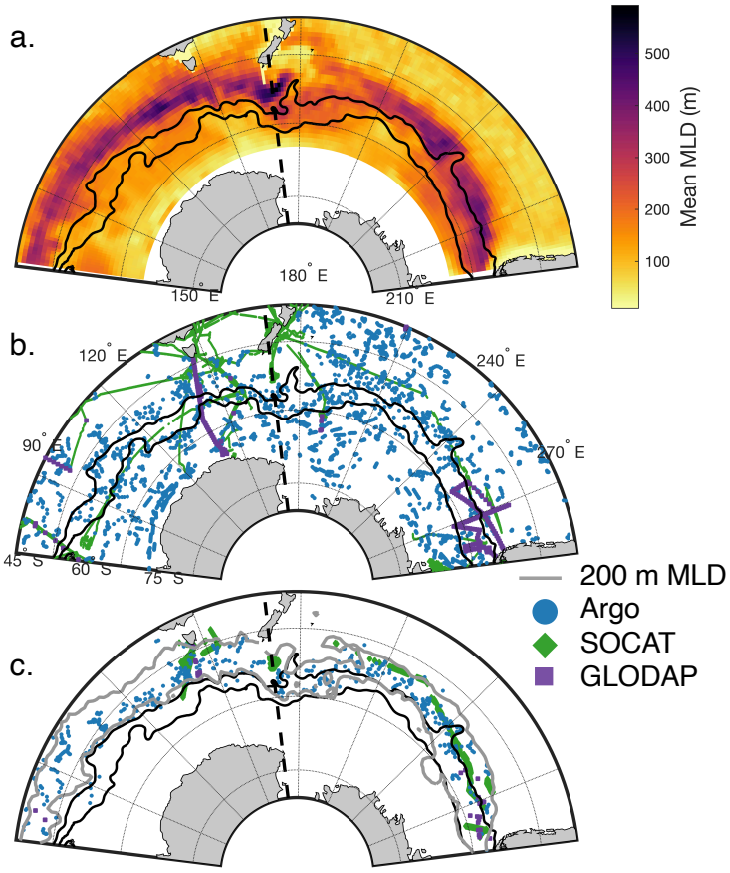

Figure 1. Wintertime mixed layer depths (MLD) and distribution of wintertime observations in the Indian and Pacific sectors of the Southern Ocean. (a) Mean winter (Aug-Sept) mixed layer depth calculated from gridded Argo product 2005-2020 (RG-Argo). (b) Map of wintertime water column biogeochemical properties (Argo floats, blue dots; GLODAP dataset since 1990, purple squares) and pCO_2 surface measurements (SOCAT dataset since 1990, green squares). (c) Same as (b), but only showing data within the SAMW density ranges in the Pacific ($26.8 \leq \sigma_\theta < 27.05$ kg m^{-3}) and Indian ($26.6 \leq \sigma_\theta < 26.9$ kg m^{-3}) basins within the wintertime mixed layer depths ≥ 200 m. The gray contour represents the mean wintertime 200 m MLD from RG-Argo indicating mode water formation regions. Black lines in all plots are the Polar Front (southern line) and the Subantarctic Front (Orsi et al. 1995). Black dashed line indicates separation between Pacific and Indian basins (170°E).

Southern Ocean mode and intermediate waters help ventilate the ocean interior with oxygen (Russell and Dickson 2003; Carter et al. 2014) and their distinctive high oxygen signature is evident as they spread into the subtropical gyre (McCartney 1977; Hanawa and Talley 2001). Modeling results indicate that SAMW has accumulated ~20% of the total ocean anthropogenic carbon inventory and gains ~28% of the annual anthropogenic carbon increase, with 60-86% of the increase coming from air-sea fluxes and the rest accumulated through interior diapycnal processes (Groeskamp et al. 2016; Iudicone et al. 2016). However, the mechanistic understanding of air-sea CO_2 fluxes that we gain from model simulations are dependent on accurate model representation of preformed mode water biogeochemical properties and resulting air-sea fluxes for which validation data has been previously unavailable.

SAMW is not homogeneous in space, but instead consists of pools of water with distinct properties that form in different locations. SAMW is then exported to the subtropics from these well-defined "hotspots" of formation following distinct pathways influenced by topography (Koch-Larrouy et al. 2010; Herraiz-Borreguero and Rintoul 2011; Li et al. 2021). While many physical processes play an important role in SAMW formation, air-sea buoyancy fluxes and

Ekman transport of cold water are generally considered to be dominant (Speer et al. 2000; Sloyan and Rintoul 2001; Rintoul and England 2002). SAMW is strongly coupled to the atmosphere and the interannual variability of wintertime atmospheric forcing governs the interannual variability and regional distribution of SAMW formation in the Pacific and Indian sectors of the Southern Ocean, as revealed by the Argo observations. In the Southern Hemisphere the extratropical atmospheric circulation has the quasi-stationary zonal wave number 3 (ZW3) pattern present in both the mean atmospheric circulation and its variability on daily, seasonal, and interannual timescales (Raphael 2004). As SAMW is strongly coupled to the atmosphere, the ZW3 can also be imprinted onto the zonal distribution of deep wintertime mixed layers associated with SAMW formation (Meijers et al. 2019; Tamsitt et al. 2020; Cerovečki and Meijers 2021). The ZW3 pattern is a prominent feature in the winter quasi-stationary mean sea level pressure (MSLP) anomalies (Cerovečki and Meijers 2021). The meridional wind anomalies introduced by these MSLP anomalies are of the opposite sign on the two flanks of each center of the MSLP anomaly, resulting in anomalously cold conditions and deep mixed layers on the flank with enhanced southerly winds, and anomalously warm conditions and shallow mixed layers on the flank with enhanced northerly winds. Thus in years with strong wintertime MSLP anomalies in the SAMW formation latitude range, deep wintertime mixed layer depth (MLD) anomalies have a dipole pattern in each of the three ocean sectors, and these MLD anomalies in the three ocean sectors tend to be in phase, which results in a more circumpolar response to the atmospheric forcing (Tamsitt et al. 2020; Cerovečki and Meijers 2021). Argo observations have also revealed that the variability of mode water volume and properties in SAMW pools is governed not only by local atmospheric forcing, but also by advective processes that transport property anomalies eastward, with a ~1 year lag between the central and southeastern Pacific (Meijers et al. 2019; Cerovečki et al. 2019).

SAMW variability is strongly linked to the dominant modes of variability in the Southern Hemisphere. The Southern Annual Mode (SAM) leads to large-scale wintertime MLD anomalies (Sallée et al. 2010), strongly influencing the volume of subducted mode water. This volume has increased over the Argo period (Gao et al. 2018; Portela et al. 2020) as mixed layers have deepened in response to a strengthening SAM (Qu et al. 2020). In the Pacific, SAMW formation is also influenced by El Niño–Southern Oscillation (ENSO), and the relative phases of the ENSO and SAM governs the interannual variability of SAMW thickness (Meijers et al. 2019).

137 In contrast to physical properties, changes in large-scale Southern Ocean biogeochemical
138 properties in response to climate variability, including those of SAMW, have primarily been
139 described using the results of model simulations. Modeling studies have linked decreased
140 contemporary Southern Ocean CO_2 fluxes and elevated surface DIC concentrations to positive
141 SAM phase through increased Ekman-driven upwelling of old waters enriched in DIC (Lenton and
142 Matear 2007; Lovenduski et al. 2007). Verdy et al. (2007) explored climate drivers of oxygen and
143 CO_2 fluxes in the Southern Ocean using a global numerical ocean model. The Pacific dipole
144 described in Meijers et al. (2019) and Cerovečki and Meijers (2021) is evident in the first EOF of
145 both oxygen and CO_2 flux variability in Verdy et al. (2007), which the authors also associate with
146 SAM. The upwelling of low oxygen water drives oceanic uptake of oxygen, so the response has
147 the opposite sign from CO_2. They find that ENSO is a secondary driver of oxygen and CO_2 flux
148 variability in the Pacific, though with a similar magnitude of induced oxygen and CO_2 fluxes and
149 a dipole structure still evident.
150 Wintertime measurements of biogeochemical tracers in the Southern Ocean are limited,
151 with most of the shipboard measurements that have historically underpinned our understanding of
152 ocean properties concentrated in a few locations (Figure 1). Therefore, despite their importance
153 for determining the distribution of carbon, nutrients, and oxygen in the ocean interior, the
154 biogeochemical properties of SAMW at the time of formation are poorly characterized. Knowing
155 water mass formation properties is key to interpreting downstream biogeochemical measurements
156 and ground-truthing the model-based interpretations of the role of SAMW in nutrient export and
157 anthropogenic carbon uptake. The impact of nutrients exported by SAMW to the global ocean on
158 air-sea carbon dioxide fluxes is determined by whether, once upwelled to the surface, those
159 nutrients are preformed or sourced from biological material that degraded sometime between
160 initial subduction and eventual re-emergence in the upper ocean. Nutrient regeneration from
161 respiration is accompanied by the release of DIC and consumption of oxygen, such that biological
162 production fueled by regenerated nutrients will either be offset by regenerated CO_2 outgassing or
163 will re-fix the regenerated DIC back to organic carbon. Preformed nutrients are not coupled to
164 regenerated DIC and can fuel net carbon uptake from the atmosphere when next upwelled to the
165 surface. Preformed nutrients are often estimated using oxygen measurements, an oxygen
166 consumption to nutrient release respiration ratio, and assumed oxygen saturation during formation.

It is therefore important to characterize oxygen and preformed nutrients present in different water masses and to understand if and how they vary in time.

Only one study has analyzed formation properties of SAMW from shipboard measurements made on individual cruises that crossed a SAMW formation region in the southeast Pacific (Carter et al. 2014). Recent deployments of profiling floats equipped with biogeochemical sensors throughout the Southern Ocean by the Southern Ocean Carbon and Climate Observations and Modeling project (SOCCOM; Johnson et al. 2017) offer a new opportunity to characterize these waters and better understand the role that SAMW plays in the global carbon cycle and production.

While mapped interpolation products are available for some biogeochemical variables (Garcia et al. 2010; Landschützer et al. 2013; Rödenbeck et al. 2013; Lauvset et al. 2016) these products are biased toward summertime measurements. For example, inclusion of float-derived pCO_2 with ship-board observations in standard mapping methods has reduced estimates of the annual Southern Ocean contemporary carbon uptake from an annual uptake of ~1.1 Pg C yr^{-1} to 0.75 ± 0.22 Pg C yr^{-1} (Bushinsky et al. 2019), primarily due to new wintertime observations. Furthermore, the wintertime formation of SAMW has strong temporal and spatial variability, leading to possible biases if properties or variability are extrapolated from too-sparse measurements (Fay et al. 2014). These float-derived year-round, vertically-resolved biogeochemical measurements for the first time enable characterization of these important water masses during formation and will provide the link between surface processes and interior ocean properties and changes. In this study we use wintertime observations from profiling floats and available shipboard measurements to characterize SAMW properties at the time of formation. Using results of an ocean state estimate we determine how these properties vary interannually and regionally prior to export into the global ocean.

2. Methods

2.1 SAMW identification

SAMW was identified from gridded Argo T&S (hereafter RG-Argo; Roemmich and Gilson 2009) using a potential vorticity (PV) threshold of PV < 40 x 10^{-12} (m $s)^{-1}$, with PV defined as $PV = f/\rho \ \partial\sigma_\theta/\partial z$, where f is the Coriolis parameter, ρ is the density of seawater, and σ_θ is the potential density (taken here to be defined relative to the surface), averaged over the years 2005-

198 2020. This PV threshold was used to identify the density range of core SAMW in the Pacific
199 (170°E to 70°W, 64°S to 45°S) and Indian (68°E to 170°E, 55°S to 30°S) ocean sectors, identified
200 as density bins (0.05 kg m^{-3}-wide spacing) containing at least 5% of total SAMW volume in an
201 annual average. We then used these density ranges throughout the rest of the study to identify
202 wintertime SAMW in each basin.
203
204 **2.2 Biogeochemical observations**
205 Biogeochemical properties of the deep wintertime mixed layers that form SAMW were
206 determined from biogeochemical Argo float observations obtained from two sources. The primary
207 dataset is observations from over 200 floats equipped with oxygen, nitrate, pH, and bio-optical
208 sensors deployed by SOCCOM since 2014 (May 2021 snapshot; Johnson et al., 2017). The
209 SOCCOM data are supplemented by the University of Washington Argo Oxygen dataset (UW
210 Argo O_2; v1.1; Drucker and Riser, 2016) that contains post-adjusted Argo oxygen data from 2003
211 to 2014. Where float data was present in both datasets the SOCCOM data were preferentially used.
212 The final dataset contains 311 floats, of which 53 contain profiles that fell within the criteria used
213 to define SAMW formation periods. A profile was determined to have sampled the SAMW
214 formation period if it fell within the density range for a given basin, was from August or
215 September, and had a calculated MLD of at least 200 m.
216 Oxygen and nitrate in the SOCCOM dataset are measured by sensors mounted on the floats
217 with stated uncertainties of 1-2 μmol kg^{-1} for oxygen and <1 μmol kg^{-1} for nitrate (Johnson et al.
218 2017). Oxygen uncertainties from the UW Argo O_2 dataset are ~1%, or ~3 μmol kg^{-1} at the
219 concentrations observed in this study. The partial pressure of carbon dioxide (pCO_2) and dissolved
220 inorganic carbon (DIC) are estimated in the SOCCOM data processed stream from measured pH
221 and an alkalinity multiple linear regression (Williams et al. 2017; Carter et al. 2018) with a
222 theoretical uncertainty of ~11 μatm for pCO_2, and ~6 μmol kg^{-1} for DIC (Williams et al. 2017,
223 2018; Johnson et al. 2017). While float observations underwent prior QC, a secondary QC was
224 performed by checking time series of temperature, salinity, oxygen, nitrate, pH, and derived pCO_2
225 in the upper 20 m for each float. Large spikes in individual properties with no accompanying
226 changes in related properties were removed from analysis (Supplemental Table S1, 116 profiles
227 removed out of 36,247 profiles total).
228

2.3 Shipboard observations and derived quantities

Shipboard bottle measurements from the Global Ocean Data Analysis Project v2.2020 (GLODAP; Key et al., 2015; Olsen et al., 2016) and underway pCO_2 data from the Surface Ocean CO_2 Atlas v2021 (SOCAT; Bakker et al., 2016) are used to supplement float observations. pCO_2 was calculated from GLODAP DIC and alkalinity using CO2SYS (van Heuven et al. 2011) and the same carbonate system constants as used by the SOCCOM project (Williams et al. 2017). MLDs are calculated for each float and ship profile using a 0.03 kg m^{-3} σ_θ change from a 10 m reference (de Boyer Montégut et al. 2004). SOCAT pCO_2 observations are underway measurements that are not associated with a vertical profile from which MLD could be calculated. Instead, SOCAT observations were matched to the closest 1° x 1° ML from objectively interpolated RG-Argo (Roemmich and Gilson 2009) MLDs .

ΔpCO_2 (surface pCO_2 minus atmospheric pCO_2) values were calculated using the atmospheric CO_2 mole fraction (xCO_2, NOAA Greenhouse Gas Marine Boundary Layer Reference; Dlugokencky et al. 2019) matched to the nearest latitude (see supplemental text S2). A correction for sea level pressure was applied using a mean annual cycle for each location calculated from a 10-year time series of National Centers for Environmental Prediction (NCEP; Kalnay et al., 1996) reanalysis sea level pressure and water vapor pressure calculated from SST and SSS (Zeebe and Wolf-Gladrow 2001). Oxygen saturation concentrations are calculated from observed temperature and salinity and García and Gordon (1992) solubility coefficients.

2.4 Biogeochemical Southern Ocean State Estimate (BSOSE)

The biogeochemical Southern Ocean State Estimate (BSOSE; Verdy and Mazloff 2017) is a coupled biogeochemical-sea-ice-ocean state estimate that assimilates physical and biogeochemical observations, including from biogeochemical profiling floats, creating a coherent picture of Southern Ocean processes that conserves mass and has closed budgets for biogeochemical properties. BSOSE is forced by optimized atmospheric reanalysis fields from ERA-Interim (Dee et al. 2011). We used iteration 135, covering 2013-2019 at 1/6° resolution, for analysis of interannual variability. Here we only analyze the spatial and temporal variability of SAMW in BSOSE output from the Pacific sector, where the spatial distribution of deep wintertime MLDs and SAMW formation regions in BSOSE iteration 135 agreed well with those from RG-

Argo. The Pacific region was additionally of interest because it reflected the impact of the strong 2015/2016 El Niño.

3. Results and discussion

3.1 SAMW formation properties

The potential density bounds established for regional SAMWs were $26.8 \leq \sigma_\theta < 27.05$ kg m^{-3} in the Pacific sector and $26.6 \leq \sigma_\theta < 26.9$ kg m^{-3} in the Indian sector. These density ranges agree well with those from the literature (e.g. Cerovečki and Meijers, 2021). We identified SAMW properties from float observations in the Pacific and Indian sectors during the time of formation using these density bounds and calculating mean mixed layer properties from August to September at the locations where the float profile mixed layer depth was at least 200 m. The depth criterion was used to isolate the deep wintertime mixed layers associated with SAMW formation from other shallower winter mixed layers, such as in areas of reventilation or seasonally formed water that does not connect to the ocean interior (Koch-Larrouy et al. 2010). The threshold value was determined by examining the individual float observations.

Pressure vs. time plots of individual floats capture the seasonal cycle of deep mixing in the winter, where the lighter density bound of SAMW outcrops at the surface and newly formed waters bring surface properties into the SAMW layer (Figure 2). As the mixed layer shoals in austral spring, these waters mix in the ocean interior with older SAMW. After leaving Pacific or Indian SAMW formation regions, floats often captured reventilation in other areas, such as float 5904695 that captured moderate wintertime ML deepening in the western Pacific in 2017 (Figure 2). The float was advected eastward by the ACC and captured the process of strong wintertime ML deepening in the Pacific in winters of 2018 and 2019. The subsequent year the float was advected through the Drake Passage into the Atlantic, where SAMW was reventilated, further modifying the properties of SAMW that were set prior to restratification and isolation from the atmosphere. The current study focuses only on the period of deep winter mixed layers and initial formation properties, leaving reventilation and other post-formation modification processes to later work.

Properties in the deep (> 200 m) winter mixed layers were first averaged in density bins within the geographical bounds of each ocean sector and then weighted by volume to calculate mean and standard deviation (Table 1). SAMW formed in the Pacific Ocean is colder and fresher, with higher oxygen, nitrate, DIC, and pCO_2 than SAMW that forms in the Indian Ocean (Table 1,

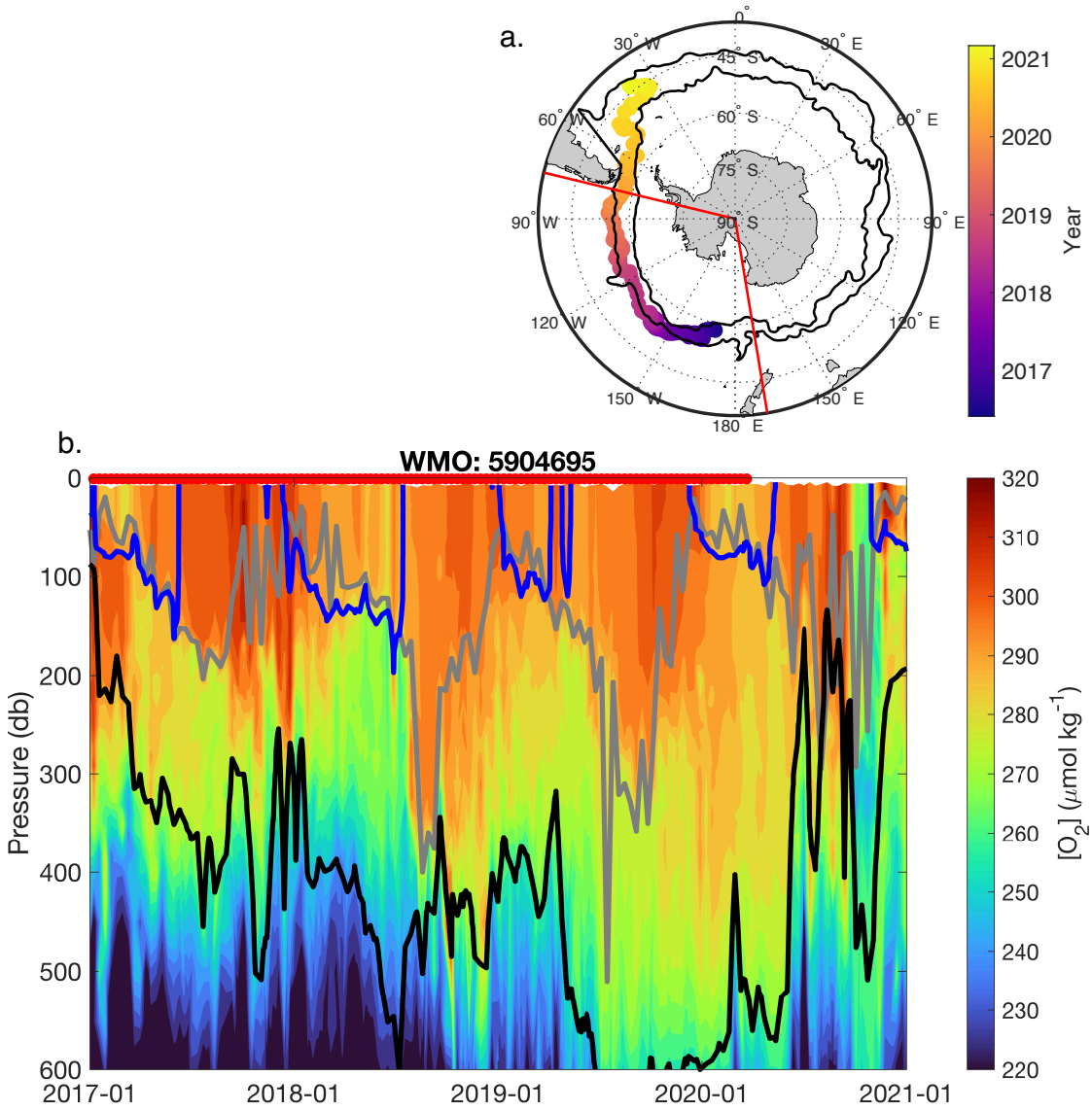

Figure 2. Trajectory and oxygen measurements from float 5904695. (a) Float 5904695 was deployed in the western Pacific in May 2016 and followed the Subantarctic Front (northern black line) as it was advected by the ACC into the Atlantic basin in 2020. Southern black line is the Polar Front. (b) Float oxygen measurements from the upper 600 m from 2017 to 2021. SAMW density bounds identified for the Pacific are shown for the lighter (blue, 26.8 kg m^{-3}) and denser (black, 27.05 kg m^{-3}) boundaries. MLD (gray) increases in the wintertime and the lighter SAMW boundary outcrops. MLs deeper than 200m were identified as waters likely to enter the ocean interior and therefore represent SAMW formation waters. This float captured both initial formation (for example in 2018 and 2019) as well as what appears to be subsequent reventilation in later years as the float passed into the Atlantic Ocean. The shallow deep SAMW boundary in 2016, 2017, and 2020 (black line) and the relatively shallow MLs indicate that these are not core SAMW formation regions, though there is some ventilation and likely modification of SAMW properties. Red dots above (b) correspond to when the float was in the Pacific sector (red lines in panel a.).

290

Table 1. Mean and standard deviation[1] of preformed properties in SAMW formation regions obtained from float observations

Region	θ (°C)	Sal. (PSS-78)	[O_2] (µmol kg^{-1})	[NO_3^-] (µmol kg^{-1})	[DIC] (µmol kg^{-1})	pCO_2 (µatm)
Pacific	5.8 ± 0.6	34.2 ± 0.1	292 ± 6.2	21.5 ± 1.2	2135.1 ± 7.5	419.3 ± 14.4
Indian	9.3 ± 1	34.6 ± 0.2	271 ± 8.2	13.3 ± 2.9	2120 ± 6.3	404.4 ± 10.7

[1]Means and standard deviations are first calculated for each 0.05 kg m^{-3} density bin, then a weighted average is calculated according to the SAMW volume fraction of each bin in the Pacific and Indian regions. The SD represents spatial and interannual variability in addition to measurement error.

Figures 3a and 3b). The relationship between potential density and each water property is nearly identical between the Pacific and Indian formation regions, indicating that the preformed property differences are primarily a function of the mean potential density of the waters formed in each region (Figure S1). The relationship between density and ocean properties determined from biogeochemical Argo observations show a generally good agreement with BSOSE for all parameters except surface pCO_2 (Figure 3, light dashed lines). Southern Ocean pCO_2 and the resulting air-sea flux is particularly hard for models to capture due to the non-linear relationship between pCO_2 and SST, DIC, and total alkalinity (Mongwe et al. 2018).

Despite capturing the overall relationship between biogeochemical properties and density shown in Figure 3a, the mean BSOSE properties differ from the Argo observations in some density classes. For instance, while BSOSE falls within the observed variability for oxygen, nitrate, and DIC in the Pacific SAMW density range, in the Indian sector BSOSE oxygen and nitrate are both higher than observations for the denser classes of SAMW. Direct comparison of BSOSE sampled at float profile locations and float observed properties for winter waters with deep (>200m) mixed layers within the regional SAMW density ranges indicates mean biases of -0.001 ± 0.72 °C, 0.07 ± 0.12 salinity, -3.4 ± 15.5 µmol kg^{-1} [O_2], 1.5 ± 2.7 µmol kg^{-1} [NO_3^-], and 0.33 ± 12.1 µmol kg^{-1} [DIC] in the Pacific and -0.47 ± 1.19 °C, -0.02 ± 0.19 salinity, 2 ± 12.6 µmol kg^{-1} [O_2], -0.1 ± 2 µmol kg^{-1} [NO_3^-], and 1.6 ± 7.5 µmol kg^{-1} [DIC] in the Indian Ocean (upper 200m average for MLs greater than 200m ± RMSE, Figure S2). The high RMSE for these comparisons reflects the difficulty for a state estimate to exactly reproduce individual observations, including differences in mixed layer depth at a specific location and the related impact on ML properties. The mean biases are small relative to the magnitude of biogeochemical property changes across the SAMW

density range. Additionally, in this study we primarily use BSOSE to explore interannual variability (Section 3.4), for which it is more important to reproduce the large-scale density property relationships than to have perfect agreement between every float profile and BSOSE output.

One of the few studies to characterize SAMW and the related AAIW properties in this region used data from a cruise in the winter of 2005 (Carter et al. 2014) to determine deep winter mixed layer properties for the SAMW that forms in the southeast Pacific. The SAMW formation properties described in Carter et al. (2014) fall on the denser end of newly formed SAMW in the

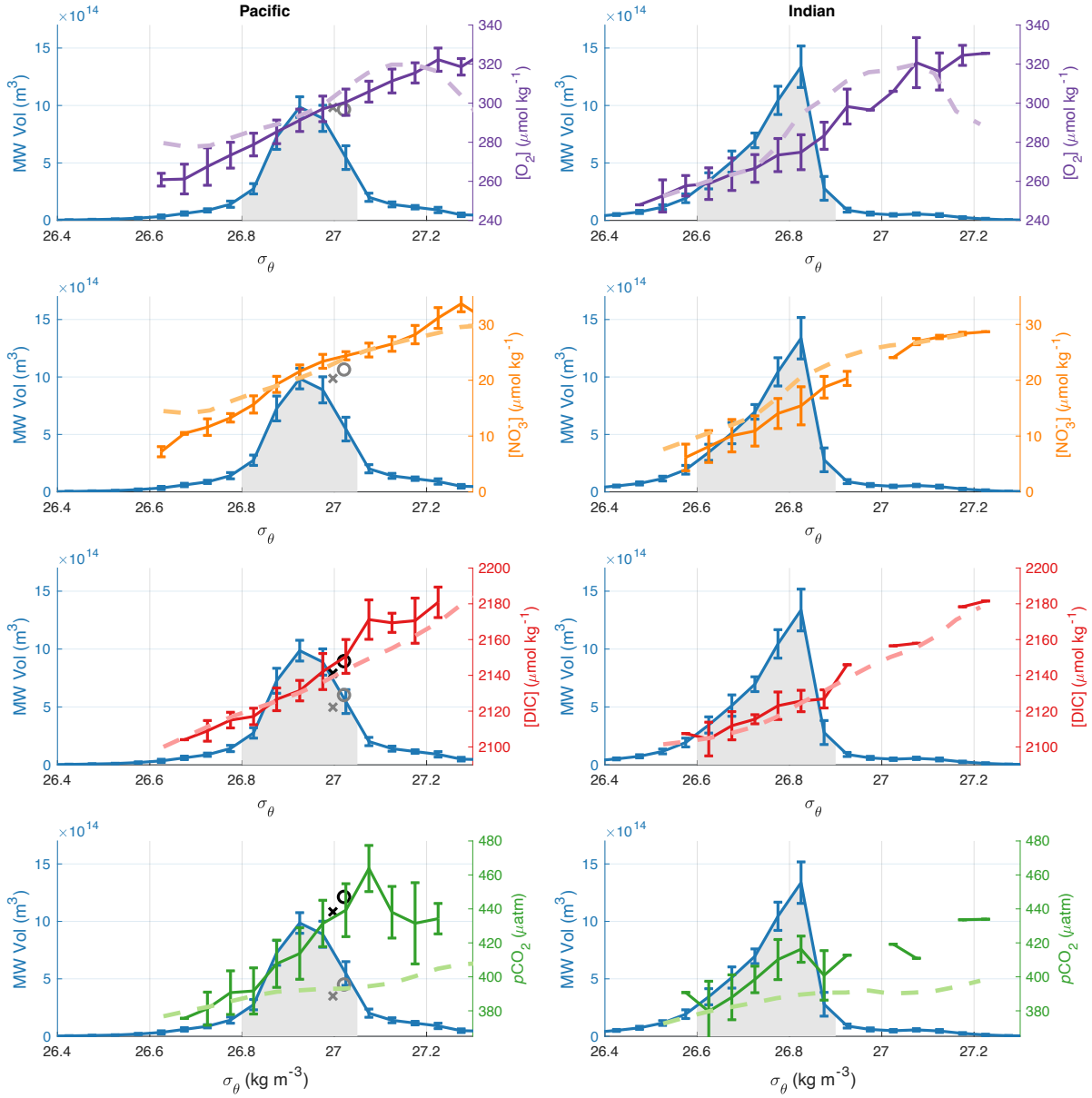

Figure 3a (previous page). Mixed layer biogeochemical properties of SAMW during wintertime formation and SAMW volume. Mode water volume and oxygen and nitrate, and estimated DIC and pCO_2 are plotted as a function of potential density. The blue curves show the monthly mean volume of water within the ML that satisfies the low potential vorticity (PV) criteria PV<40×10^{-12} s^{-1} m^{-1}, obtained from the RG-Argo data set, for months August and September, 2005-2020, and binned into 0.05 kg m^{-3} wide density bins with the standard deviations indicating the interannual variability. The shaded areas under the volume curves indicates the density bins that contain at least 5% of SAMW by volume. Colored lines with error bars indicate the average properties ± 1 SD from biogeochemical floats, binned into the same 0.05 kg m^{-3} wide density bins. Volume and property data are from mixed layers that exceed 200 m. Dashed lines are the Aug-Sept mean biogeochemical properties from five-day averaged output from the Biogeochemical Southern Ocean State Estimate (BSOSE) and time averaged over years 2013-2019 where five-day averaged MLDs are deeper than 200m. Overlaid on the Pacific plots are markers indicating the SAMW formation properties identified in Carter et al. (2014) from their "North- Deep Mixed Layer Water" (northwest SAMW outcrop region, gray x's) and "South-Deep Mixed Layer Water" (southeast SAMW outcrop region, gray o's) samples. The Carter et al. (2014) [NO_3^-] is an average of 2.9 µmol kg^{-1} lower than this study's observations in the same density range. Adjusting the Carter et al. (2014) DIC and pCO_2 for the equivalent difference in organic matter (plus change in alkalinity due to organic matter respiration and SST difference for pCO_2) yields DIC and pCO_2 shown by the black x's and o's. The longitude range of the Indian Ocean sector is 68-170°E, and the Pacific sector 170-290°E.

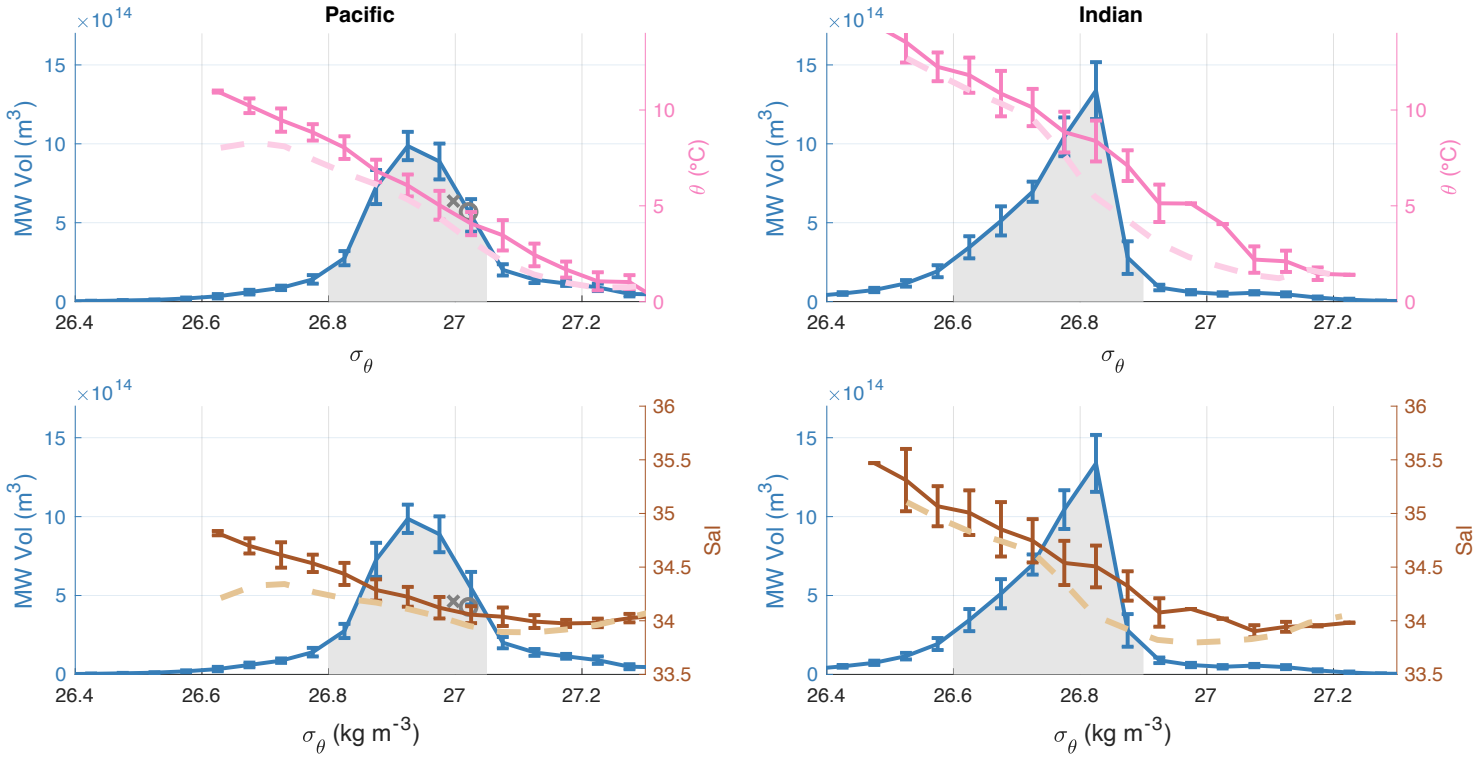

Figure 3b. Equivalent to Fig 3a but for potential temperature and salinity.

Pacific, as expected since the southeast Pacific SAMW is the coldest and freshest. The Carter et al. (2014) estimates are 0.9-1.4 °C colder and 0.05-0.01 PSU fresher than the mean Pacific SAMW properties described in this study. Samples of θ, salinity, and [O_2] fall within ± 1 SD of the property-density relationships described in Figure 3a and 3b (gray symbols in Figure 3). The Carter et al. (2014) [NO_3^-] is ~2.9 μmol kg^{-1} lower than the [NO_3^-] observed in this study, indicating that either the SAMW formation region sampled in the present study has a greater fraction of older water with a stronger signal of respiration or that less biological production has occurred since that water has been at the surface, either of which could result in a higher [NO_3^-] value. The [DIC] and pCO_2 calculated from the Carter et al. (2014) [DIC] and alkalinity are correspondingly lower than observed values. Correcting for the different amount of biological activity using an assumed Redfield stoichiometry of 106C: 16N and recalculating the [DIC] and pCO_2 (in the latter case, also correcting for SST and the biological impacts on alkalinity) yields values that are within the uncertainty of our observed property relationships with density (Figure 3, black symbols). This indicates that there is no fundamental disagreement between the carbonate system values derived from these float measurements and those observed by Carter et al. (2014). The [NO_3^-] and [DIC] differences between the Carter et al. (2014) results and the current study may additionally indicate variability or change on a multi-year time scale and warrants further exploration with longer time-series of observations or model output. The wide range of biogeochemical properties across the density range of newly formed SAMW illustrates the need for observations that span the entire density and spatial extent of newly formed SAMW to fully characterize properties at the time of formation.

Carter et al. (2021) used ocean observations and interior ocean mixing pathways to estimate preformed properties of oxygen, nitrate, silica, phosphate, and total alkalinity throughout the ocean interior. To compare Carter et al. (2021) to the current values for SAMW we applied the same geographic bounds for the Pacific and Indian regions to the Carter et al. (2021) preformed properties and masked results using the RG-Argo mean winter MLD criteria of >200m. This yielded preformed properties at 200m depth of 284.8 ± 13.3 μmol kg^{-1} [O_2] and 22.3 ± 3.9 μmol kg^{-1} [NO_3^-] in the Pacific and 257.1 ± 8.2 μmol kg^{-1} [O_2] and 13.4 ± 3.6 μmol kg^{-1} [NO_3^-] in the Indian Ocean (mean ± 1 SD). The differences in preformed [O_2] between Carter et al. (2021) and the current study are of a similar magnitude to our mean SAMW preformed oxygen undersaturation and therefore important to reconcile in future work. Comparison between the

results of Carter et al. (2021) and the current study is limited by the lack of density information from the Carter et al. (2021) results, so it is unclear whether the possible bias between these results is meaningful or an artifact of interpretation.

The relative properties of Pacific and Indian formation regions can be broadly interpreted using the property and density relationship described in Figure 3 as differences in mixing fraction of TW and AAIW/CDW in SAMW formation. The Indian SAMW formation region, which is located further north than the formation region in the Pacific, displays a greater influence of TW coming from the subtropics with higher temperatures and lower nutrients and carbon, whereas the Pacific SAMW formation region has a greater influence of upwelled deep water, with high carbon and nutrients, and cold temperatures. Oxygen concentrations follow the north-south temperature gradient, as oxygen air-sea exchange is fast relative to that of CO_2, allowing the mixed layer to come close to solubility equilibrium with the atmosphere rather than being controlled by the initial $[O_2]$ of the mixing water masses. This interpretation that preformed biogeochemical properties are dependent on the mixing fraction is consistent with our physical understanding of how mode waters form in these two regions. An early analysis of the Southern Ocean State Estimate found SAMW forming in the Indian Ocean to have a greater fraction of volume transformed from the lighter (TW) waters than the SAMW forming in the Pacific (Cerovečki and Mazloff 2016). Using data from biogeochemical Argo floats, Fernández Castro et al. (2022) similarly documented the influence of salty, nutrient-poor subtropical waters on SAMW formation properties which decreases from the Indian to Pacific regions and is an important factor influencing the pre-formed nutrient content of SAMW.

The difference between the mean SAMW biogeochemical properties in the Indian and Pacific regions shown in Figure 3a indicates that, at a minimum, properties of newly formed SAMW will change depending on the relative volumes of water formed in the Pacific and Indian SAMW formation regions or within different density classes in the eastern and western areas of each region. During the Argo time period in both the Indian and Pacific sectors of the Southern Ocean, the SAMW volume trends showed a two-layer density structure, with an upper layer volume increase and a lower layer volume decrease (Kolodziejczyk et al. 2019; Portela et al. 2020). The large range of properties within the SAMW density range in each of these two ocean sectors, shown in Figure 3, suggests that this SAMW volume variability is likely accompanied by similar variability of biogeochemical properties. Understanding the link between the density of SAMW

formed and the impact on subducted biogeochemical properties may be critical for projection of future Southern Ocean conditions as the predicted poleward intensification of Southern Ocean winds may impact mode water subduction rates differently in the Indian and Pacific formation regions (Downes et al. 2017). While we now have sufficient data to describe the mean SAMW formation properties in the Pacific and Indian Oceans, these basin-wide averages likely mask the intra-basin differences and longer-term variability documented for the physical properties. Current observational coverage alone is of insufficient density and length to convincingly explore intra-basin biogeochemical differences.

3.2. Oxygen saturation during formation

SAMW is undersaturated in oxygen at the time of formation in both the Pacific and Indian formation regions (Table 2, Figure 4). Wintertime SAMW $\Delta[O_2]$, or the observed oxygen concentration minus saturation concentration ($\Delta[O_2] = [O_2]_{\text{measured}} - [O_2]_{\text{satuturation}}$, $\mu mol\ kg^{-1}$), is negative in almost all individual float observations and in all August and September averages, consistent with the sparse observations available in these wintertime locations in the GLODAP v2.2020 shipboard dataset. Pacific SAMW has a mean $\Delta[O_2]$ of -11.1 ± 2.3 µmol kg^{-1} during formation and Indian SAMW has a mean $\Delta[O_2]$ of -7.7 ± 2.7 µmol

Table 2. Mean $\Delta[O_2]$ and ΔpCO_2 of SAMW at the time of formation

	[1]$\Delta[O_2]$ (µmol kg^{-1})			[2]ΔpCO_2 (µatm)			
Region	**Argo**	**GLODAP**	**Combined Argo & GLODAP**	**Argo**	**GLODAP**	**SOCAT**	**Combined Argo & SOCAT**
Pacific	-11.1 ± 2.3	-12.2 ± 1.7	-11.1 ± 2.3	23.9 ± 14.7	20.1 ± 0.5	5.7 ± 3.6	16.1 ± 14.5
Indian	-7.9 ± 2.4	-6 ± 4.3	-7.7 ± 2.7	9.3 ± 11.7	-14 ± 16.4	-6.4 ± 7.5	0.1 ± 12.2

[1] $\Delta[O_2] = [O_2]_{ML,observed} - [O_2]_{saturation}$; O_2 saturation calculated as a function of temperature and salinity (Garcia and Gordon, 1992)

[2] $\Delta pCO_2 = pCO_{2,surf} - X_{CO_2} \times (\frac{SLP}{1013.25} - pH_2O)$; X_{CO2} from the NOAA Greenhouse Gas Marine Boundary Layer Reference (Dlugokencky et al. 2019), sea level pressure (SLP) in mbar, pH_2O calculated as a function of temperature and salinity (Zeebe and Wolf-Gladrow, 2001).

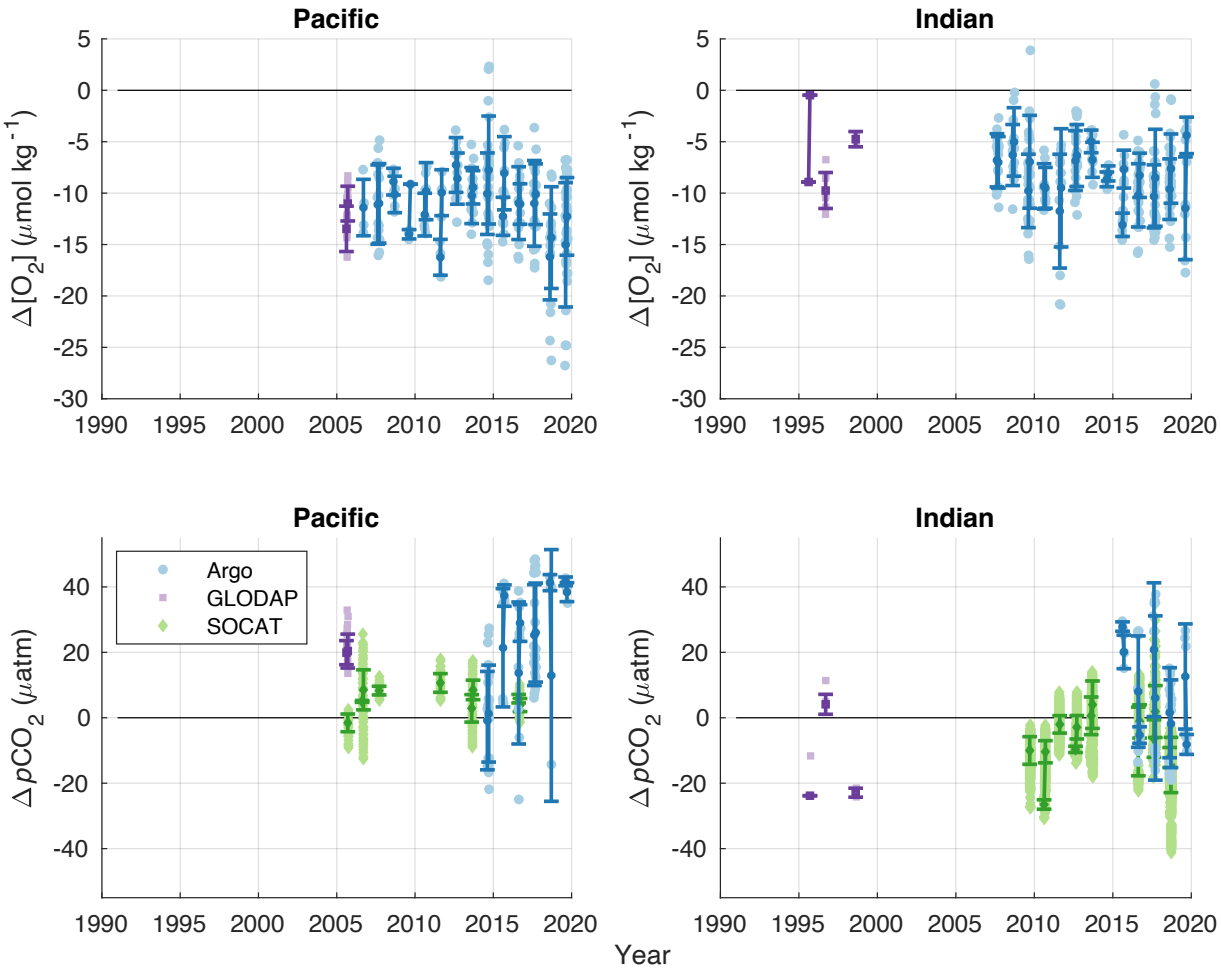

401

Figure 4. ΔpCO_2 and $\Delta[O_2]$ in SAMW formation regions from Argo floats and shipboard observations. (Top row) $\Delta[O_2]$ is calculated using the mixed layer average oxygen concentration from Argo floats (blue circles) and GLODAP shipboard measurements (purple squares) and is not corrected for local atmospheric pressure, reflecting the use of interior oxygen measurements relative to saturation concentration with an assumed atmospheric pressure of 1 atm. (Bottom row) ΔpCO_2 values from SOCAT pCO_2 measurements (green diamonds), Argo ph-derived pCO_2 estimates, and GLODAP DIC and alkalinity measurements using CO2SYS (van Heuven et al., 2011). SOCAT data are from near-surface underway systems, Argo data from the shallowest observation (typically 5-7m depth), and GLODAP data are from the upper 25m due to data availability. ΔpCO_2 for all data sources were calculated from NOAA ESRL atmospheric CO_2 values, corrected for water vapor pressure, and a 2011-2020 climatological sea level pressure. ΔpCO_2 from Argo floats is higher (indicates more outgassing or less oceanic uptake) than recent SOCAT ΔpCO_2 but represents samples made over a wider range of SAMW waters.

402 kg^{-1} (Table 2, average of float and GLODAP data). During the formation period, high winds drive
403 strong gas exchange and an oxygen flux into the ocean to relieve undersaturation. $\Delta[O_2]$ is
404 calculated with an assumption of a standard sea level pressure (SLP) of 1013.25 mbar (1 atm).
405 Wintertime SLP in the Southern Ocean is typically below 1013.25 mbar and accounting for the
406 mean winter SLP in the Pacific and Indian formation regions would reduce oxygen undersaturation
407 by ~30% (Text S4). The fact that the waters stay undersaturated throughout the wintertime
408 formation period indicates that a combination of surface cooling by atmospheric heat loss and
409 continued entrainment of low oxygen sub-surface waters is maintaining undersaturation
410 throughout the time of water mass formation and subduction.

411 Undersaturation of oxygen at the time of water mass formation has long been discussed as
412 a source of error in interpreting interior ocean oxygen measurements but estimates of preformed
413 oxygen undersaturation have primarily come from model results. Model results have indicated
414 significant oxygen undersaturation during deep water formation in the North Atlantic and Southern
415 Ocean (Ito et al. 2004; Duteil et al. 2013). The assumption that water masses are in equilibrium
416 with atmospheric oxygen underpins one of the most common uses of interior ocean oxygen
417 measurements, calculation of apparent oxygen utilization (AOU; $\mathrm{AOU} = [\mathrm{O_2}]_{\mathrm{saturation}} -$
418 $[\mathrm{O_2}]_{\mathrm{measured}}, \mu\mathrm{mol\,kg^{-1}}$), where $[O_2]_{saturation}$ is determined from temperature and salinity
419 dependent oxygen solubility (García and Gordon 1992). This quantity is key to determining
420 preformed quantities through the stoichiometric relationship between the consumption of oxygen
421 and release of nutrients and DIC during respiration (e.g.. Mackay and Watson 2021). Oxygen
422 utilization rates (OUR) describe the average respiration in a parcel of water by combining apparent
423 oxygen utilization (AOU) and an age tracer and, again, typically rely on the assumption that
424 preformed oxygen is at saturation. While one study (Koeve and Kähler 2016) found that
425 undersaturation in preformed oxygen did not make a large difference in calculated OUR due to
426 other offsetting errors, this was based on a single model and did not have the observations to
427 evaluate if that model accurately represented preformed biogeochemical properties.

428 The increasing number of oxygen-equipped profiling floats deployed throughout the ocean
429 is enabling the first observational studies of wintertime oxygen saturation over large areas. The
430 first basin-scale description of mixed layer $\Delta[O_2]$ and air-sea oxygen fluxes over several years was
431 also conducted in the Southern Ocean using Argo-oxygen floats, finding broad surface regions of
432 undersaturated wintertime waters but without focusing on specific water masses or ventilation

433 regions (Bushinsky et al. 2017). In the Labrador Sea, Wolf et al. (2018) used Argo-oxygen floats
434 to quantify significant undersaturation in Labrador Sea water at the time of formation that would
435 bias AOU and derived biogeochemical properties. In the study that estimated preformed properties
436 globally (Carter et al. 2021), errors in calculations of AOU were greatest in water formed in the
437 Southern Ocean and in the North Pacific due to the strong degree of wintertime oxygen
438 undersaturation in these regions. Broecker and Peng (1982) introduced the concept of True Oxygen
439 Utilization (TOU), which is the difference between preformed oxygen concentration and the
440 observed concentration, to account for the expected undersaturation during water formation events.
441 Here we show for the first time in SAMW using direct observations of the wintertime formation
442 that SAMW is undersaturated in oxygen when it leaves the ocean surface, altering the
443 interpretation of observations in this water mass throughout the ocean interior and allowing for the
444 calculation of TOU.

445 It is important to consider oxygen sensor accuracy and method of calibration when
446 comparing to shipboard observations as some float oxygen data have been adjusted to match
447 shipboard data. Oxygen data in the SOCCOM dataset (36 out of 53 floats) are calibrated using
448 either atmospheric oxygen as a reference point or using initial shipboard casts if atmospheric data
449 are not available (Johnson et al. 2017; Maurer et al. 2021). Deployments do not occur during the
450 winter and these float oxygen data are therefore independent of the GLODAP shipboard data
451 presented in Figure 4 and Table 2. Oxygen data in the UW Argo O_2 dataset are re-processed using
452 a two-point correction (one near-surface and one deep calibration value). The near-surface values
453 are air measurements (if available) or World Ocean Database (WOD, Garcia et al. 2010) mean
454 values. Surface reference values for the WOD were only used if the water was close to saturation
455 (98-101% O_2 saturation). It is therefore unlikely that any of the shipboard observations shown in
456 Figure 4 were used in the calibration. Therefore, while the uncertainty of oxygen data corrected to
457 WOD is higher than air-calibrated data, these also represent independent observations from the
458 GLODAP data. Uncertainties for the SOCCOM (1-2 μmol kg^{-1}) and UW Argo O_2 (~3 μmol kg^{-1})
459 datasets are much smaller than the mean offset and SD of the data shown here and are therefore
460 unlikely to be a major factor in the undersaturation found in the pre-formed oxygen estimates.
461
462
463

3.3 Carbon dioxide saturation during formation

Mean monthly derived ΔpCO_2 (surface pCO_2 minus atmospheric pCO_2, Text S2) determined only from float observations is positive in the Pacific (22.5 ± 13.5 µatm) formation region and slightly positive in the Indian SAMW formation region (9.5 ± 12.9 µatm) (Table 2; Figure 4, bottom). In both the Pacific and Indian SAMW formation regions the ΔpCO_2 calculated from float observations overlaps with, but is generally higher than, either direct shipboard measurements (SOCAT) or derived ΔpCO_2 from paired DIC and alkalinity measurements (GLODAP). SOCAT pCO_2 observations are direct measurements with accuracy better than 5 µatm (including quality flags A-D, Lauvset et al. 2017), while the float-derived pCO_2 estimates utilize a recently developed technique with a theoretical uncertainty of approximately ± 11 µatm (Williams et al. 2017). Float observations have previously shown higher pCO_2 during the winter than has been recorded in the SOCAT database (Gray et al. 2018; Williams et al. 2018). This elevated wintertime pCO_2 yields a reduction in the Southern Ocean (south of 35°S) CO_2 sink in 2015-2017 from 1.1 Pg C yr^{-1} based on SOCAT data alone to 0.75 Pg C yr^{-1} using a combined SOCAT and SOCCOM dataset (Bushinsky et al. 2019). These results have been challenged, most recently by a study using atmospheric CO_2 measurements and atmospheric transport models to constrain the Southern Ocean sink (Long et al. 2021), which yielded a stronger Southern Ocean CO_2 sink, though with overlapping uncertainties between the atmospheric constraint and the SOCCOM and SOCAT float-based pCO_2 estimates in all months for which atmospheric data existed and potential complications from previously documented interannual and decadal variability.

The key question for average values of ΔpCO_2 or air-sea fluxes is whether averaged float estimates of pCO_2 are accurate, not whether individual observations are precise. Crossover comparisons between ship and float pCO_2 have indicated a possible high bias of float pCO_2 by ~4 µatm (Fay et al. 2018; Gray et al. 2018; Williams et al. 2018), smaller than the differences between the Argo and SOCAT mean values in Table 2. An updated crossover comparison with the addition of a filter eliminating crossover density differences >0.03 kg m^{-3} yields a mean float-derived pCO_2 bias of -1.86 ± 15.8 µatm (SOCAT minus floats, n = 52, Supplemental Figure S3). Recent work evaluating float pCO_2 against shipboard observations indicates that float pCO_2 may be high by ~6 µatm (Mackay and Watson 2021; Wu et al. 2022) and comparison against aircraft-derived CO_2 fluxes indicate that float-derived outgassing is too strong in the winter due to high-biased pCO_2

values. This makes it unlikely that an error in the pCO_2 estimation method is responsible for the entire 17-20 µatm difference in ΔpCO_2 between the mean Argo and SOCAT values shown in Fig. 4, though it may be responsible for some of the offset.

A large portion of the difference between the SAMW formation ΔpCO_2 from SOCAT and Argo is more likely due to the differences in sample distribution within each of these formation regions. The strong coupling of density and biogeochemical properties seen in Figure 3 highlights the importance of sampling the full range of densities. Previous work demonstrating spatial variability in physical formation properties of SAMW indicates that spatial variations in biogeochemical properties are also likely to exist. Histograms of the relative frequency of ΔpCO_2, longitude, σ_θ, and θ of mode water formation region observations by the Argo and SOCAT datasets identify differences in the sample distributions of these observations (Figure 5). In the Pacific, SOCAT-determined ΔpCO_2 has a peak of ~0 µatm and a tail toward positive values. The SOCAT observations are primarily from ~170°E, at the very western edge of the Pacific basin, while one cruise crossed the Pacific in 2006. This results in observations that are primarily from σ_θ 26.88 – 26.9 kg m^{-3} and θ of 7.26 – 7.94 °C. Float observations cover a broader range of locations within the Pacific and are consequently spread more evenly across the SAMW density range. SOCAT sample coverage in the Indian Ocean is primarily from cruises originating from Tasmania and do not cover the large formation regions in the central and western Indian Ocean. There are relatively few GLODAP-derived ΔpCO_2 values in either basin, so our best estimate of the ΔpCO_2 for each region is an average of monthly values from the SOCAT and Argo datasets, yielding 16.1 ± 14.5 µatm ΔpCO_2 in the Pacific and 0.1 ± 12.2 µatm ΔpCO_2 in the Indian Ocean. If we applied a uniform 6 µatm bias to the float-derived pCO_2 values, it would lower the mean ΔpCO_2 at formation to 12.7 ± 12.8 µatm in the Pacific and -3.1 ± 10.7 µatm in the Indian Ocean.

The entire Southern Ocean is a significant sink for contemporary carbon, mainly driven by the increase in atmospheric anthropogenic carbon and resulting oceanic anthropogenic uptake (Mikaloff Fletcher et al. 2006; Gruber et al. 2009b; DeVries 2014). Much of this anthropogenic carbon is both stored in and exported by mode and intermediate waters (Sabine et al. 2004; Mikaloff Fletcher et al. 2006; Álvarez et al. 2009; Gruber et al. 2009a; Sabine and Tanhua 2010). Model-derived calculations of anthropogenic carbon uptake use the difference in ocean carbon fluxes and accumulation between model runs that do and do not include increasing atmospheric carbon to determine uptake rates of anthropogenic carbon (Iudicone et al. 2011, 2016; Groeskamp

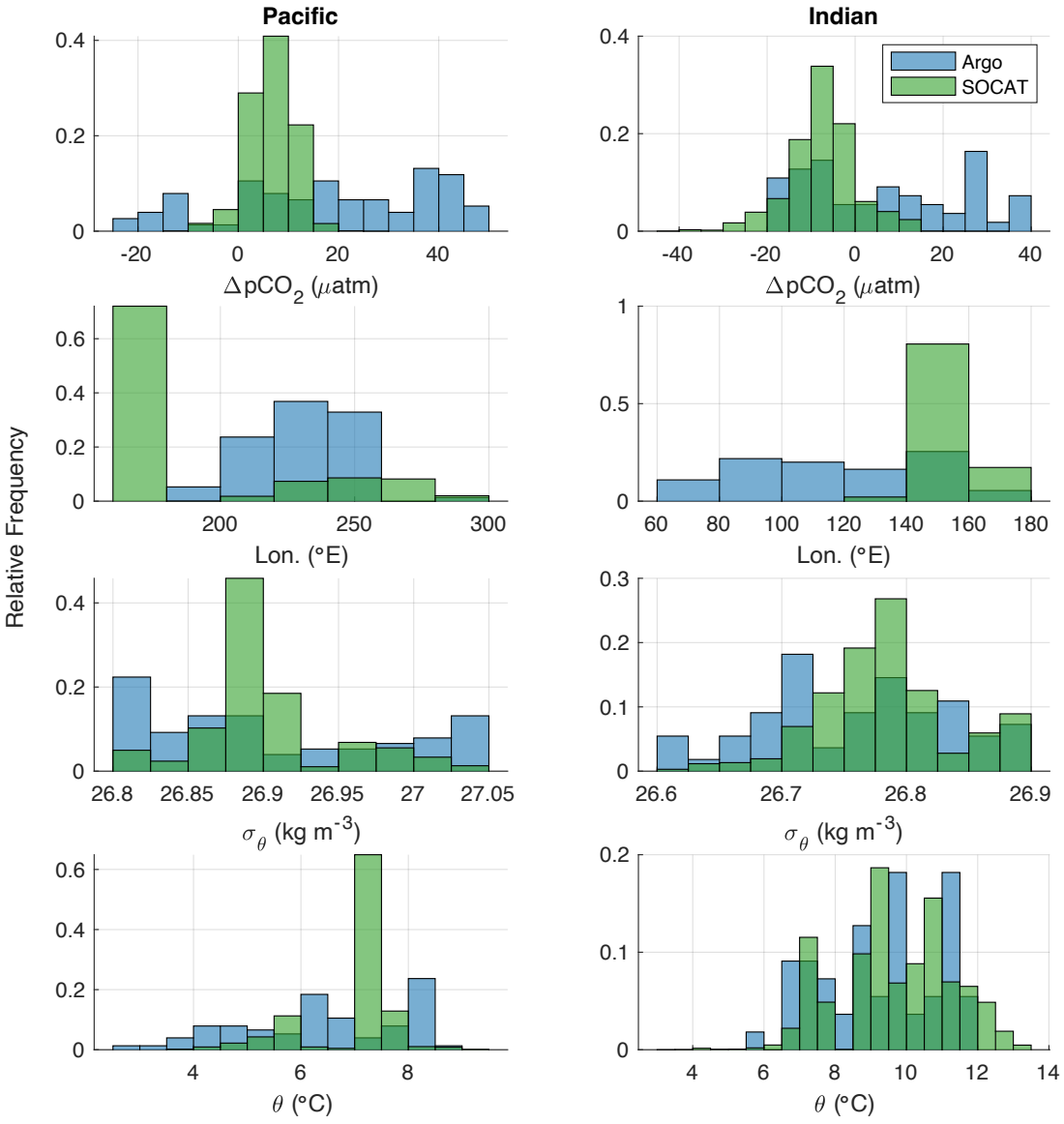

526

Figure 5. Properties associated with ΔpCO_2 calculated from SOCAT and Argo. Relative frequency histograms of calculated ΔpCO_2 and the associated longitude, potential density, and potential temperature for SAMW formation properties in the Pacific and Indian Oceans. SOCAT ΔpCO_2 values are primarily from narrow geographic regions in the Pacific sector near New Zealand and in the Indian sector near Tasmania. Biogeochemical Argo data are spread across the sectors, with more distributed density and potential temperature values as well. ΔpCO_2 for SOCAT is similarly within relatively narrow ranges for both sectors, while Argo-derived ΔpCO_2 overlaps with and, on average, is higher than SOCAT ΔpCO_2. GLODAP-derived ΔpCO_2 and associated properties are not shown, as they represent a much smaller sample range and were not included in the property averages (Table 2).

et al. 2016). This approach relies on an accurate representation of water mass properties and the physical and biogeochemical processes that influence the carbonate system in models, which have been shown to have difficulty in capturing the seasonal cycle of pCO_2 and air-sea CO_2 fluxes in the Southern Ocean (Mongwe et al. 2018). If the models do not accurately capture contemporary carbon uptake, then the anthropogenic carbon fluxes and storage will be biased.

Recent work attempting to constrain the magnitude of wintertime outgassing in the Southern Ocean (Gray et al. 2018; Bushinsky et al. 2019; Mackay and Watson 2021; Sutton et al. 2021; Long et al. 2021) makes it all the more important to understand the mechanisms that could contribute to total Southern Ocean uptake of contemporary and anthropogenic carbon. A ΔpCO_2 during formation that is near or above zero indicates that SAMW does not contribute to the total Southern Ocean contemporary carbon uptake during formation. Given the increase in atmospheric pCO_2 from anthropogenic emissions, it is likely that these waters would have been a pre-industrial source of carbon to the atmosphere and the current near-zero ΔpCO_2 represents an anthropogenic carbon sink. It is clear from observed accumulation of anthropogenic carbon in the ocean interior (Sabine et al. 2004; Mikaloff Fletcher et al. 2006; Sabine and Tanhua 2010; Gruber et al. 2019a) that SAMW is important for the storage of anthropogenic carbon and export to the ocean interior, but the modeling work that has sought to elucidate whether SAMW accumulates anthropogenic carbon through surface or interior processes has not had robust observations for validation (Iudicone et al. 2011; Groeskamp et al. 2016). Here we provide both the mean biogeochemical properties and their distribution with respect to water mass density that can be used to validate model property distributions and representation of contemporary carbon fluxes, thereby improving future estimates of the magnitude and mechanisms of anthropogenic carbon uptake and partitioning of uptake between surface and interior processes.

3.4 Spatial and interannual variability of SAMW formation properties

Almost 15 years of Argo observations have provided invaluable information about strong interannual and spatial variability of SAMW physical properties. Argo observations have revealed that the strong wintertime MLD anomalies in the Pacific, Indian, and Atlantic sectors that develop in some years , and are associated with SAM and ENSO, tend to be out of phase in the western and eastern parts of ocean sectors (Meijers et al. 2019; Tamsitt et al. 2020; Cerovečki and Meijers 2021). In years with anomalously strong formation of colder and denser varieties of SAMW in the

558 eastern parts of the Indian and Pacific sectors, the formation of warmer and lighter varieties of
559 SAMW in the western part of both ocean sectors is anomalously weak, enhancing the net cooling
560 and densification in each ocean sector. Conditions reverse in years with the preferential formation
561 of warmer and lighter varieties of SAMW (Cerovečki and Meijers 2021). Anomalies that develop
562 in the western part of one ocean sector can subsequently be advected by the ACC to arrive
563 approximately one year later to the eastern SAMW formation region of the same ocean sector
564 (Meijers et al. 2019; Cerovečki et al. 2019). This pattern of an east-west dipole in MLD anomalies
565 and propagation of strong anomalies is evident in the BSOSE Aug-Sept time-mean MLD (Figure
566 6). During the 2013-2019 period of BSOSE model simulation analyzed here, the strongest MLD
567 anomalies developed in 2016 when a strong El Niño event coincided with a strong positive SAM
568 early in the year (Figure 6a). By austral winter 2016, both indexes transitioned to strongly negative
569 (Meijers et al. 2019). The in-phase atmospheric modes resulted in anomalously deep and cold
570 wintertime mixed layers in the central Pacific, and anomalously shallow and warm mixed layers
571 in the southeast Pacific (Meijers et al. 2019; Cerovečki et al. 2019).
572 In addition to the previously described temperature anomalies (not shown) associated with
573 the 2016 MLD anomalies, BSOSE displays high DIC and high NO_3^- in the central Pacific and low
574 DIC and NO_3^- in the eastern Pacific (Figure 6b). The opposite pattern is observed in 2015, when
575 anomalously shallow MLs in the central Pacific were associated with low DIC and low NO_3^-, while
576 anomalously deep MLs in the eastern Pacific entrained high DIC and NO_3^- waters. These anomaly
577 maps suggest a link between SAM, ENSO, and biogeochemical anomalies, but the BSOSE time
578 series is too short for more definitive attribution in the current study. Due this relatively short time
579 period we chose to investigate interannual winter property anomalies rather than e.g. carrying out
580 an EOF analysis, though an initial EOF analysis produced qualitatively similar results.
581 A time-series of the wintertime (Aug-Sept) mean ML property anomalies within the Pacific
582 SAMW density range ($26.8 \leq \sigma_\theta < 27.05$ kg m^{-3}) considered separately in the central (45-64°S,
583 170-246°E) and southeast (45-64°S, 246-290°E) Pacific reveals a similar dipole pattern of DIC,
584 nitrate, and oxygen as found in prior work considering physical properties (Figure 7). These two
585 regions of the Pacific are not entirely out of phase, as the biogeochemical properties during the
586 formation time period are not only governed by the local surface forcing that drives MLD
587 anomalies, but also the properties from water formed in prior years incorporated through

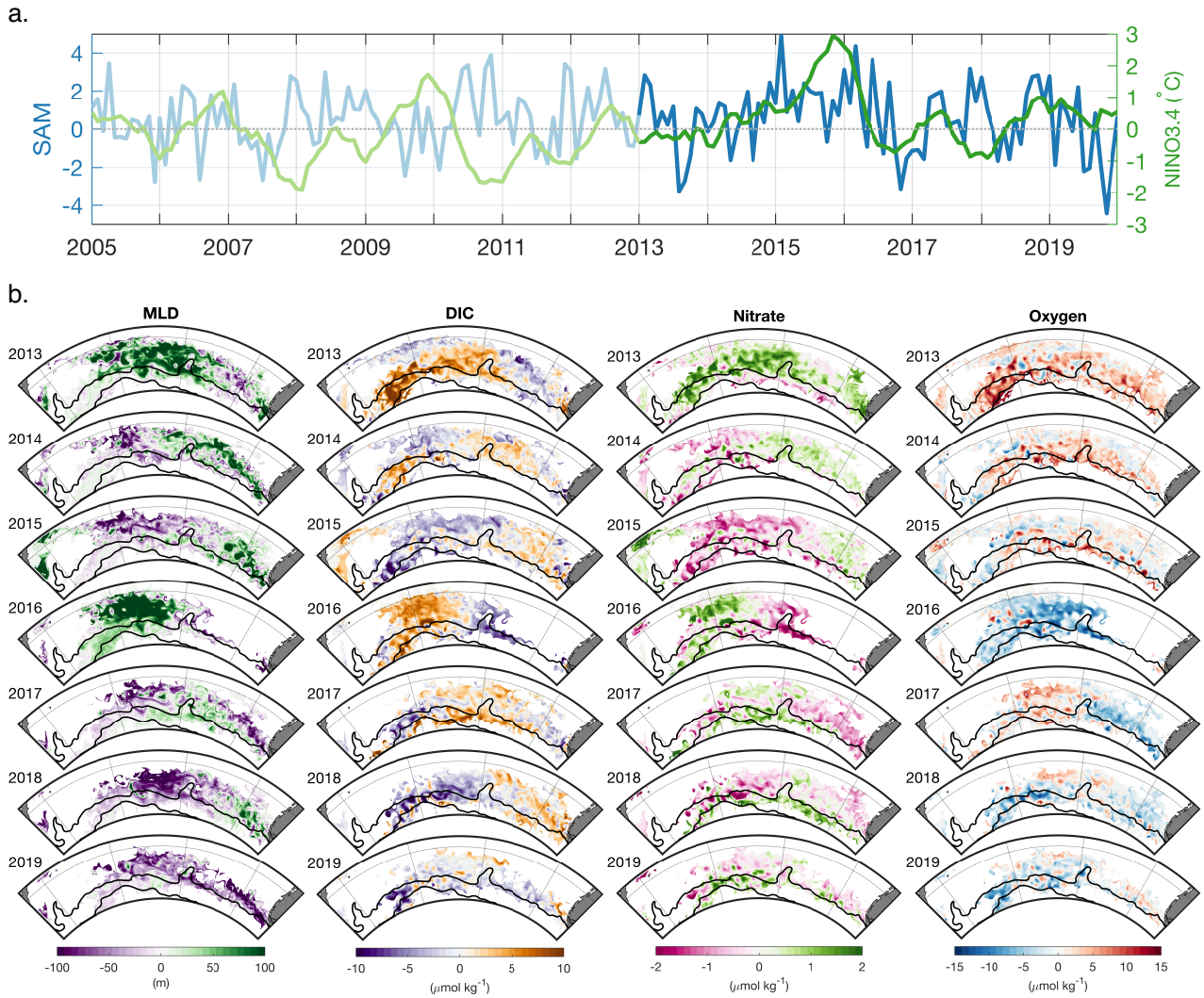

Figure 6. Time series of ENSO, SAM, and BSOSE winter anomalies in MLD, DIC, nitrate, and oxygen. (a) SAM (blue) and ENSO (green) indices are highlighted during the years covered by BSOSE. (b) Winter (Aug-Sept) anomalies for MLD, DIC, nitrate, and oxygen demonstrate the combined influence of ENSO and SAM. Years and regions with deep MLD anomalies (green) are associated with higher DIC (orange) and nitrate (green). Spatial patterns of anomalies demonstrate a dipole between the central Pacific and southeast Pacific in many years, similar to a previously demonstrated pattern in SST, and Salinity (Cerovečki and Meijers, 2021).

entrainment and lateral induction. The mean property anomalies of the Pacific are more closely correlated with central Pacific than the southeast Pacific due to the larger volume of water formed in the central Pacific, in agreement with observational work by Cerovečki and Meijers (2021).

Oxygen time variability is more complicated than that of nitrate and DIC, as the fast gas exchange rate moves to restore air-sea equilibrium and replenish waters that are initially deficient in oxygen but have low temperatures and high solubility. In some years, such as 2016 when the

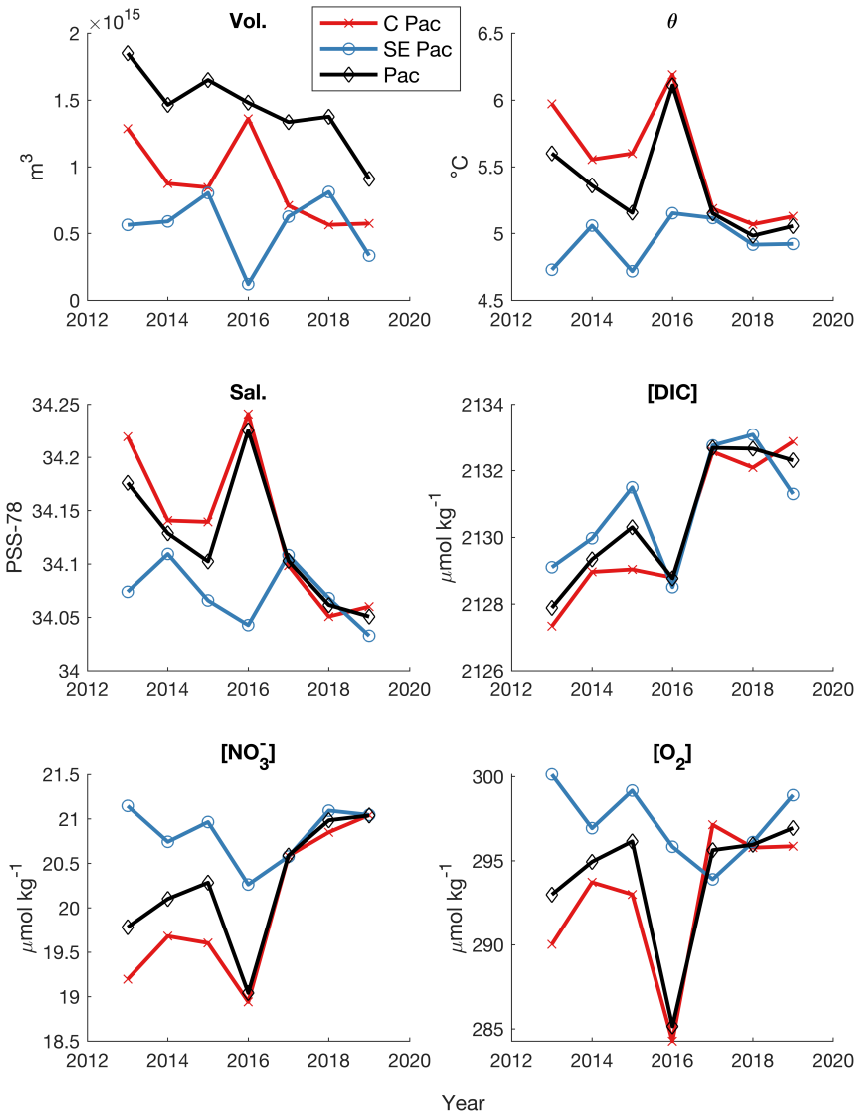

Figure 7. SAMW Pacific formation properties in BSOSE. Anomalies are mean winter (Aug-Sept) ML properties in the Pacific SAMW density range ($26.8 \leq \sigma_\theta < 27.05$ kg m^{-3}). Anomalies are calculated for the central (red line, 45-64°S, 170-246°E), southeast (blue, 45-64°S, 246-290°E), and overall Pacific (black, 45-64°S, 170-290°E) regions.

strong El Niño and strongly positive SAM combined to produce anomalously deep MLs in the central Pacific, the oxygen anomaly is negative, indicating that the entrainment signal was strong and persisted through the SAMW formation period (Figs. 6 and 7). In other years, such as 2013, deep MLs in the central Pacific are associated with positive oxygen anomalies. This dichotomy reflects the competing processes that impact oxygen in the upper ocean. In years with strong heat loss to the atmosphere, cooler temperatures will increase the solubility, which, coupled with strong winds driving high air-sea gas exchange rates, will tend to increase the oxygen concentration in the surface ocean. On the other hand, deeper mixing will entrain more low-oxygen water from below and the increased volume of the mixed layer will slow the change in oxygen concentration

for a given air-sea flux. Years with reduced air-sea heat loss in the winter and shallower MLs are characterized by warmer temperatures and lower solubility but also less entrainment of low-oxygen waters. A plot of SAMW oxygen concentration against potential temperature for the Pacific and Pacific sub-regions reveals that the main signal is a fairly consistent offset relative to oxygen saturation of which approximately 1/3 is due to low SLP (Figure S4), implying that not only do oxygen concentrations closely follow interannual temperature changes, but also that the balance of the above processes leads to a consistent $\Delta[O_2]$ despite large changes in MLD and temperature. Both the magnitude of the $\Delta[O_2]$ offset and the lack of variability in BSOSE are consistent with float and ship-board observations (Figure 4). (Wolf et al. 2018)

Interestingly, the differences in biogeochemical property anomalies observed between the central and southeastern Pacific are more pronounced during the first half of the BSOSE time series than after 2016 (Figure 7). Physical and biogeochemical properties across the Pacific become more uniform after the 2016 El Niño and remain so through 2017, 2018, and 2019 (Figure 7, difference between the central Pacific (red line, 45-64°S, 170-246°E), and southeast Pacific (blue line, 45-64°S, 246-290°E)). This is likely caused in part by advection of anomalies from the central to southeast Pacific following the strong 2016 El Nino, as previously shown for temperature anomalies using Argo data (Cerovečki and Meijers 2021). Similar advection of anomalies of biogeochemical properties from west to east Pacific SAMW formation regions is evident in Figure 6. This propagation of signals across the entire Pacific formation region is suggested by the apparent movement of anomalies from west to east in Figure 6. Advection of biogeochemical anomalies in BSOSE is more prominent when viewed in a Hovmöller diagram of the volume-weighted average upper ocean anomalies in the region where Aug-Sept MLs exceed 150m (Figure S5). Similar advective signals have been described in Argo observations of physical properties (Cerovečki and Meijers 2021) and previously in modeled temperature, salinity, and air-sea fluxes of oxygen and carbon dioxide (Verdy et al. 2007).

We are left with a framework where interannual variability in the biogeochemical properties of newly formed SAMW is influenced by a mix of local atmospheric forcing combined with the lateral induction of prior signals into the wintertime mixed layer. This mix of processes agrees with prior work on SAMW physical properties (Meijers et al. 2019; Cerovečki et al. 2019; Li et al. 2021) and a study demonstrating that surface fluxes are often not strong enough to change the physical properties of SAMW, due to the memory in the large volume of sub-surface water

(Rintoul and England 2002). Advective propagation of anomalies can sometimes be interrupted by sufficiently large forcing events, but many biogeochemical anomalies do transit the entire Pacific SAMW formation region (Figure S5).

4. Conclusions

Here we use biogeochemical Argo float observations spanning a seven-year period to characterize for the first time the regional distribution of SAMW formation properties in the Pacific and Indian sectors, finding that the colder, fresher SAMW that forms in the Pacific is also higher in oxygen, nitrate, DIC, and pCO_2 than SAMW that forms in the Indian Ocean. The differences in formation properties between the Pacific and Indian Oceans reflect the density of SAMW formed in each region. The distribution of wintertime properties against density is consistent in both sectors, indicating that these property distributions predominantly represent a continuum of source water mass mixing between thermocline water, upwelled circumpolar deep water, AAIW, and re-entrained SAMW.

In both the Pacific and Indian sectors, SAMW is undersaturated in oxygen at the time of formation, with slightly stronger undersaturation present in the Pacific formation regions. This undersaturation must be taken into account when calculating derived quantities that normally assume oxygen saturation at the time of water mass formation. This observed undersaturation appears fairly constant over the observed time period and matches results from biogeochemical ocean state estimate BSOSE that suggest some consistent balance between undersaturation due to cooling or entrainment and replenishment by air-sea gas exchange that is maintained despite large interannual differences in oxygen concentration and SST.

There are large differences between the mean ΔpCO_2 of newly formed SAMW estimated from profiling floats and that measured by underway shipboard observations. Float estimates of winter ΔpCO_2 are on average ~17 μatm higher in this study than the limited SOCAT observations from the same formation regions, part of which could be due to a systemic bias in float-derived pCO_2. However, float observations are geographically more uniformly distributed over the SAMW formation regions, sampling a wider range of properties than has been measured from shipboard observations. The bulk of these differences can be explained by the different sample distribution in the two datasets. During the wintertime formation period, SAMW has a positive ΔpCO_2 (average of SOCAT and float datasets) in the Pacific and a near neutral ΔpCO_2 in the Indian

formation region. This indicates that SAMW formation is not directly driving air-sea uptake of contemporary CO_2. The biogeochemical observations here provide for the first time the comparison data necessary to determine if models used to understand how anthropogenic carbon enters the ocean interior through mode and intermediate waters are accurately representing ocean biogeochemistry during mode water formation.

There are sufficient float biogeochemical observations to constrain mean wintertime formation properties but there are not currently enough to investigate sub-regional or interannual variability. We thus used BSOSE output to explore spatial and temporal SAMW variability, focusing on the Pacific SAMW formation region. In the Pacific the link between climate modes of variability and SAMW response is the strongest and BSOSE representation of the spatial distribution of deep winter mixing in the Pacific was more similar to these from the RG-Argo than in the Indian sector. Comparison between this study and Cerovečki and Meijers (2021) indicates that BSOSE well reproduces the large-scale response of the MLD to SAM and ENSO, showing the dipole pattern of variability between the central and southeast Pacific. BSOSE also accurately represents the relationships between biogeochemical properties and water mass density that we find in observations, giving good confidence that it can used to develop our understanding of the link between climate forcing and biogeochemical property variability in SAMW formation waters.

Interannual variability in the central and southeast Pacific biogeochemical formation properties display a see-saw pattern similar to that previously found in observations of physical properties. The suggested dipole pattern of biogeochemical properties relates well to the corresponding pattern in mixed layer depth and entrainment of deeper waters, with high nitrate and high DIC in regions and years with deep mixed layer anomalies and low nitrate and low DIC when the mixed layer is anomalously shallow. We expect that with more biogeochemical observations made in the Southern Ocean, these patterns will become evident in the observations as well. Interannual variability in oxygen concentration closely follows changes in ML temperature with a consistent undersaturation indicating that ML waters do not have time to equilibrate with the atmosphere regardless of whether the MLDs are anomalously deep or shallow.

Future work should focus on decomposing interannual variability in biogeochemical signals between those driven by local forcing and the influence of multi-year advective signals. A detailed understanding of the variability present in SAMW formation regions will help to understand how sensitive the interior volume is to changes in volume and properties of the

individual formation regions and how strongly those variations are either modulated by the total interior SAMW volume or transported to the rest of the ocean.

SAMW is a critical water mass for the uptake of anthropogenic carbon and transport of oxygen and nutrients into the ocean interior. Improving our understanding of SAMW biogeochemical properties and their variability is of fundamental importance for improving our interpretation of interior ocean measurements, providing better validation for models, and therefore enabling new understanding of how SAMW functions in these global biogeochemical cycles.

Acknowledgements:

Float data were collected and made freely available by the Southern Ocean Carbon and Climate Observations and Modeling (SOCCOM) Project funded by the National Science Foundation, Division of Polar Programs (NSF PLR -1425989 and OPP-1936222), supplemented by NASA, and by the International Argo Program and the NOAA programs that contribute to it. The Argo Program is part of the Global Ocean Observing System. The Surface Ocean CO_2 Atlas (SOCAT) is an international effort, endorsed by the International Ocean Carbon Coordination Project (IOCCP), the Surface Ocean Lower Atmosphere Study (SOLAS) and the Integrated Marine Biosphere Research (IMBeR) program, to deliver a uniformly quality-controlled surface ocean CO_2 database. The many researchers and funding agencies responsible for the collection of data and quality control are thanked for their contributions to SOCAT. The specific SOCAT data used in this study were contributed by PIs K. Currie, A. Sutton, T. Trull, C. Sabine, T. Takahashi, C. Sweeney, S. C. Sutherland, T. Newberger, D. R. Munro, B. Tilbrook, J. Akl, and C. Neill. SOCAT data from the R/V Tangaroa were collected by the National Institute of Water and Atmospheric Research (funded by the New Zealand Ministry of Business, Innovation and Employment). SOCAT data from the R/V Gould and R/V Palmer were funded by the National Oceanic and Atmospheric Administration through the Global Ocean Monitoring and Observing Program and the Office of Oceanic and Atmospheric Research and by the National Science Foundation (grant numbers PLR 1341647 and 1543457). SOCAT underway data from Tilbrook, Akl and Neill were sourced through Australia's Integrated Marine Observing System (IMOS) – IMOS is enabled by the National Collaborative Research Infrastructure Strategy (NCRIS). Specific GLODAP data were collected on the R/Vs Knorr, Aurora Australis, Malcolm

Baldrige, and M.-Dufresne. SMB was supported by NASA grants NNX17AI73G and 80NSSC22K0156 and benefited from support by the NOAA Climate Program Office's Climate Observations and Monitoring, Climate Variability and Predictability, and Global Ocean Monitoring and Observation programs (NA21OAR4310260). IC was supported by NASA grants 80NSSC22K0156 and 80NSSC19K1115. This is SOEST contribution XXXX.

Conflict of Interest Statement

The authors have no conflicts of interest to declare.

Open Research

Datasets used in this paper are from these references and the associated repositories:

Biogeochemical float data are from the May 2021 SOCCOM snapshot (Johnson et al, 2017; doi.org/10.6075/J0T43SZG), along with the Drucker and Riser (2016) UW Argo Oxygen dataset which is now included in the Argo dataset (https://argo.ucsd.edu/data/data-from-gdacs/). Gridded Argo product by Roemmich and Gilson (2009) is available from https://argo.ucsd.edu/data/argo-data-products/. Argo data were collected and made freely available by the International Argo Program and the national programs that contribute to it (http://doi.org/10.17882/42182, http://www.argo.ucsd.edu, http://argo.jcommops.org).

Shipboard data are from SOCAT v2021 (Bakker et al., 2016; https://www.socat.info/index.php/data-access/) and GLODAP v2.2020 (Key et al., 2015; Olsen et al., 2016; https://www.glodap.info/index.php/merged-and-adjusted-data-product/).

Analysis and plotting code for this study are available at https://doi.org/10.5281/zenodo.7349405 (Bushinsky and Cerovečki 2022).

752 **References**
753
754 Álvarez, M., C. Lo Monaco, T. Tanhua, and others. 2009. Estimating the storage of
755 anthropogenic carbon in the subtropical Indian ocean: A comparison of five different
756 approaches. Biogeosciences **6**: 681–703. doi:10.5194/bg-6-681-2009
757 Bakker, D. C. E., B. Pfeil, C. S. Landa, and others. 2016. A multi-decade record of high-quality
758 fCO2 data in version 3 of the Surface Ocean CO2 Atlas (SOCAT). Earth Syst. Sci. Data **8**:
759 383–413. doi:10.5194/essd-8-383-2016
760 de Boyer Montégut, C., G. Madec, A. S. Fischer, A. Lazar, and D. Iudicone. 2004. Mixed layer
761 depth over the global ocean: An examination of profile data and a profile-based
762 climatology. J. Geophys. Res. **109**: C12003. doi:10.1029/2004JC002378
763 Broecker, W. S., and T. H. Peng. 1982. Tracers in the Sea., Lamont-Doherty Earth Observatory.
764 Bushinsky, S., and I. Cerovečki. 2022. Subantarctic Mode Water Biogeochemical Formation
765 Properties and Interannual Variability, analysis and plotting code
766 (v1.1.1).doi:10.5281/zenodo.7349405
767 Bushinsky, S. M., A. R. Gray, K. S. Johnson, and J. L. Sarmiento. 2017. Oxygen in the Southern
768 Ocean From Argo Floats: Determination of Processes Driving Air-Sea Fluxes. J. Geophys.
769 Res. Ocean. **122**: 8661–8682. doi:10.1002/2017JC012923
770 Bushinsky, S. M., P. Landschützer, C. Rödenbeck, and others. 2019. Reassessing Southern
771 Ocean Air-Sea CO 2 Flux Estimates With the Addition of Biogeochemical Float
772 Observations. Global Biogeochem. Cycles **33**: 1370–1388. doi:10.1029/2019GB006176
773 Carter, B. R., R. A. Feely, S. K. Lauvset, and others. 2021. Preformed Properties for Marine
774 Organic Matter and Carbonate Mineral Cycling Quantification. Global Biogeochem. Cycles
775 **35**: 64–75. doi:10.1029/2020GB006623
776 Carter, B. R., R. A. Feely, N. L. Williams, and others. 2018. Updated methods for global locally
777 interpolated estimation of alkalinity, pH, and nitrate. Limnol. Oceanogr. Methods **16**: 119–
778 131. doi:10.1002/lom3.10232
779 Carter, B. R., L. D. Talley, and A. G. Dickson. 2014. Mixing and remineralization in waters
780 detrained from the surface into Subantarctic Mode Water and Antarctic Intermediate Water
781 in the southeastern Pacific. J. Geophys. Res. Ocean. **119**: 4001–4028.
782 doi:10.1002/2013JC009355
783 Cerovečki, I., and M. R. Mazloff. 2016. The spatiotemporal structure of diabatic processes
784 governing the evolution of Subantarctic Mode Water in the southern ocean. J. Phys.
785 Oceanogr. **46**: 683–710. doi:10.1175/JPO-D-14-0243.1
786 Cerovečki, I., and A. J. S. Meijers. 2021. Strong quasi-stationary wintertime atmospheric surface
787 pressure anomalies drive a dipole pattern in the Subantarctic ModeWater formation. J.
788 Clim. 1–44. doi:10.1175/JCLI-D-20-0593.1
789 Cerovečki, I., A. J. S. Meijers, M. R. Mazloff, and others. 2019. The Effects of Enhanced Sea Ice
790 Export from the Ross Sea on Recent Cooling and Freshening of the Southeast Pacific. J.
791 Clim. **32**: 2013–2035. doi:10.1175/JCLI-D-18-0205.1
792 Dee, D. P., S. M. Uppala, A. J. Simmons, and others. 2011. The ERA-Interim reanalysis:
793 Configuration and performance of the data assimilation system. Q. J. R. Meteorol. Soc. **137**:
794 553–597. doi:10.1002/qj.828
795 DeVries, T. 2014. The oceanic anthropogenic CO 2 sink: Storage, air-sea fluxes, and transports
796 over the industrial era. Global Biogeochem. Cycles **28**: 631–647.
797 doi:10.1002/2013GB004739

798 Dlugokencky, E. J., K. W. Thoning, P. M. Lang, and P. P. Tans. 2019. NOAA Greenhouse Gas
799 Reference from Atmospheric Carbon Dioxide Dry Air Mole Fractions from the NOAA
800 ESRL Carbon Cycle Cooperative Global Air Sampling Network.
801 Downes, S. M., C. Langlais, J. P. Brook, and P. Spence. 2017. Regional impacts of the westerly
802 winds on Southern Ocean mode and intermediate water subduction. J. Phys. Oceanogr. **47**:
803 2521–2530. doi:10.1175/JPO-D-17-0106.1
804 Drucker, R., and S. C. Riser. 2016. In situ phase-domain calibration of oxygen Optodes on
805 profiling floats. Methods Oceanogr. **17**: 1–34. doi:10.1016/j.mio.2016.09.007
806 Duteil, O., W. Koeve, A. Oschlies, and others. 2013. A novel estimate of ocean oxygen
807 utilisation points to a reduced rate of respiration in the ocean interior. Biogeosciences **10**:
808 7723–7738. doi:10.5194/bg-10-7723-2013
809 Fay, A. R., N. S. Lovenduski, G. A. Mckinley, and others. 2018. Utilizing the Drake Passage
810 Time-series to understand variability and change in subpolar Southern Ocean pCO 2.
811 Biogeosciences Discuss. doi:https://doi.org/10.5194/bg-2017-489
812 Fay, A. R., G. A. McKinley, and N. S. Lovenduski. 2014. Southern Ocean carbon trends:
813 Sensitivity to methods. Geophys. Res. Lett. **41**: 6833–6840. doi:10.1002/2014GL061324
814 Fernández Castro, B., M. Mazloff, R. G. Williams, and A. C. Naveira Garabato. 2022.
815 Subtropical contribution to Sub-Antarctic Mode Waters. Geophys. Res. Lett.
816 doi:10.1029/2021gl097560
817 Friedlingstein, P., M. W. Jones, M. O'Sullivan, and others. 2019. Global Carbon
818 Budget 2019. Earth Syst. Sci. Data **11**: 1783–1838. doi:10.5194/essd-11-1783-2019
819 Gao, L., S. R. Rintoul, and W. Yu. 2018. Recent wind-driven change in Subantarctic Mode
820 Water and its impact on ocean heat storage. Nat. Clim. Chang. **8**: 58–63.
821 doi:10.1038/s41558-017-0022-8
822 García, H. E., and L. I. Gordon. 1992. Oxygen solubility in seawater: Better fitting equations.
823 Limnol. Oceanogr. **37**: 1307–1312. doi:10.4319/lo.1992.37.6.1307
824 Garcia, H. E., R. A. Locarnini, T. P. Boyer, and others. 2010. World Ocean Atlas 2009 Volume
825 3: Dissolved Oxygen, Apparent Oxygen Utilization, and Oxygen Saturation.
826 Gray, A. R., K. S. Johnson, S. M. Bushinsky, and others. 2018. Autonomous Biogeochemical
827 Floats Detect Significant Carbon Dioxide Outgassing in the High-Latitude Southern Ocean.
828 Geophys. Res. Lett. **45**: 9049–9057. doi:10.1029/2018GL078013
829 Groeskamp, S., A. Lenton, R. Matear, B. M. Sloyan, and C. Langlais. 2016. Anthropogenic
830 carbon in the ocean—Surface to interior connections. Global Biogeochem. Cycles **30**:
831 1682–1698. doi:10.1002/2016GB005476
832 Gruber, N., D. Clement, B. R. Carter, and others. 2019a. The oceanic sink for anthropogenic CO
833 2 from 1994 to 2007. Science (80-.). **363**: 1193–1199. doi:10.1126/science.aau5153
834 Gruber, N., S. C. Doney, S. R. Emerson, and others. 2009a. Adding oxygen to Argo: Developing
835 a global in-situ observatory for ocean deoxygenation and biogeochemistry. Ocean Obs '09.
836 Gruber, N., M. Gloor, S. E. Mikaloff Fletcher, and others. 2009b. Oceanic sources, sinks, and
837 transport of atmospheric CO 2. Global Biogeochem. Cycles **23**: n/a-n/a.
838 doi:10.1029/2008GB003349
839 Gruber, N., P. Landschützer, and N. S. Lovenduski. 2019b. The Variable Southern Ocean
840 Carbon Sink. Ann. Rev. Mar. Sci. **11**: 159–186. doi:10.1146/annurev-marine-121916-
841 063407
842 Hanawa, K., and L. Talley. 2001. Mode waters, p. 373–386. *In* International Geophysics.
843 Hartin, C. A., R. A. Fine, B. M. Sloyan, and others. 2011. Formation rates of Subantarctic mode

water and Antarctic intermediate water within the South Pacific. Deep. Res. Part I Oceanogr. Res. Pap. **58**: 524–534. doi:10.1016/j.dsr.2011.02.010

Herraiz-Borreguero, L., and S. R. Rintoul. 2011. Subantarctic mode water: Distribution and circulation. Ocean Dyn. **61**: 103–126. doi:10.1007/s10236-010-0352-9

van Heuven, S. M. A. C., D. Pierrot, J. W. B. Rae, E. Lewis, and D. W. R. Wallace. 2011. Matlab program developed for CO2 system calculations. 530.

Ito, T., M. J. Follows, and E. A. Boyle. 2004. Is AOU a good measure of respiration in the oceans? Geophys. Res. Lett. **31**: n/a-n/a. doi:10.1029/2004GL020900

Iudicone, D., K. B. Rodgers, Y. Plancherel, and others. 2016. The formation of the ocean's anthropogenic carbon reservoir. Sci. Rep. **6**: 35473. doi:10.1038/srep35473

Iudicone, D., K. B. Rodgers, I. Stendardo, and others. 2011. Water masses as a unifying framework for understanding the Southern Ocean Carbon Cycle. Biogeosciences **8**: 1031–1052. doi:10.5194/bg-8-1031-2011

Johnson, K. S., J. N. Plant, L. J. Coletti, and others. 2017. Biogeochemical sensor performance in the SOCCOM profiling float array. J. Geophys. Res. Ocean. **122**: 6416–6436. doi:10.1002/2017JC012838

Kalnay, E., M. Kanamitsu, R. Kistler, and others. 1996. The NCEP/NCAR 40-Year Reanalysis Project. Bull. Am. Meteorol. Soc. **77**: 437–471. doi:http://dx.doi.org/10.1175/1520-0477(1996)077<0437:TNYRP>2.0.CO;2

Key, R. M., A. Olsen, S. van Heuven, and others. 2015. Global Ocean Data Analysis Project, Version 2 (GLODAPv2). ORNL/CDIAC-162, NDP-093. doi:10.3334/CDIAC/OTG.NDP093_GLODAPv2

Koch-Larrouy, A., R. Morrow, T. Penduff, and M. Juza. 2010. Origin and mechanism of Subantarctic Mode Water formation and transformation in the Southern Indian Ocean. Ocean Dyn. **60**: 563–583. doi:10.1007/s10236-010-0276-4

Koeve, W., and P. Kähler. 2016. Oxygen utilization rate (OUR) underestimates ocean respiration: A model study. Global Biogeochem. Cycles **30**: 1166–1182. doi:10.1002/2015GB005354

Kolodziejczyk, N., W. Llovel, and E. Portela. 2019. Interannual Variability of Upper Ocean Water Masses as Inferred From Argo Array. J. Geophys. Res. Ocean. **124**: 6067–6085. doi:10.1029/2018JC014866

Landschützer, P., N. Gruber, D. C. E. Bakker, and others. 2013. A neural network-based estimate of the seasonal to inter-annual variability of the Atlantic Ocean carbon sink. Biogeosciences **10**: 7793–7815. doi:10.5194/bg-10-7793-2013

Lauvset, S., K. Currie, N. Metzl, and others. 2017. SOCAT Quality Control Cookbook: for SOCAT version 7. SOCAT. doi:http://dx.doi.org/10.25607/OBP-1665

Lauvset, S. K., R. M. Key, A. Olsen, and others. 2016. A new global interior ocean mapped climatology: The 1° × 1° GLODAP version 2. Earth Syst. Sci. Data **8**: 325–340. doi:10.5194/essd-8-325-2016

Lenton, A., and R. J. Matear. 2007. Role of the Southern Annular Mode (SAM) in Southern Ocean CO2 uptake. Global Biogeochem. Cycles **21**: 1–17. doi:10.1029/2006GB002714

Li, Z., M. H. England, S. Groeskamp, I. Cerovečki, and Y. Luo. 2021. The Origin and Fate of Subantarctic Mode Water in the Southern Ocean. J. Phys. Oceanogr. 2951–2972. doi:10.1175/jpo-d-20-0174.1

Long, M. C., B. B. Stephens, K. McKain, and others. 2021. Strong Southern Ocean carbon uptake evident in airborne observations. Science (80-.). **374**: 1275–1280.

doi:10.1126/science.abi4355
Lovenduski, N. S., N. Gruber, S. C. Doney, and I. D. Lima. 2007. Enhanced CO 2 outgassing in the Southern Ocean from a positive phase of the Southern Annular Mode. Global Biogeochem. Cycles **21**: n/a-n/a. doi:10.1029/2006GB002900
Mackay, N., and A. Watson. 2021. Winter air-sea CO 2 fluxes constructed from summer observations of the Polar Southern Ocean suggest weak outgassing . J. Geophys. Res. Ocean. doi:10.1029/2020jc016600
Maurer, T. L., J. N. Plant, and K. S. Johnson. 2021. Delayed-Mode Quality Control of Oxygen, Nitrate, and pH Data on SOCCOM Biogeochemical Profiling Floats. Front. Mar. Sci. **8**: 1–20. doi:10.3389/fmars.2021.683207
McCartney, M. 1982. The subtropical recirculation of mode waters. J. Mar. Res **40**: 427–464.
McCartney, M. S. 1977. Subanarctic Mode Water, p. 103–119. *In* M. Angel [ed.], A Voyage of Discovery: George Deacon 70th Anniversary Volume.
Meijers, A. J. S., I. Cerovečki, B. A. King, and V. Tamsitt. 2019. A See-Saw in Pacific Subantarctic Mode Water Formation Driven by Atmospheric Modes. Geophys. Res. Lett. **46**: 13152–13160. doi:10.1029/2019GL085280
Mikaloff Fletcher, S. E., N. Gruber, A. R. Jacobson, and others. 2006. Inverse estimates of anthropogenic CO 2 uptake, transport, and storage by the ocean. Global Biogeochem. Cycles **20**: n/a-n/a. doi:10.1029/2005GB002530
Mikaloff Fletcher, S. E., N. Gruber, A. R. Jacobson, and others. 2007. Inverse estimates of the oceanic sources and sinks of natural CO2 and the implied oceanic carbon transport. Global Biogeochem. Cycles **21**: 1–19. doi:10.1029/2006GB002751
Mongwe, N. P., M. Vichi, and P. M. S. Monteiro. 2018. The seasonal cycle of p CO 2 and CO 2 fluxes in the Southern Ocean: diagnosing anomalies in CMIP5 Earth system models. Biogeosciences **15**: 2851–2872. doi:10.5194/bg-15-2851-2018
Morrison, A. K., T. L. Frölicher, and J. L. Sarmiento. 2015. Upwelling in the Southern Ocean. Phys. Today **68**: 27–32. doi:10.1063/PT.3.2654
Morrison, A. K., D. W. Waugh, A. M. Hogg, D. C. Jones, and R. P. Abernathey. 2022. Ventilation of the Southern Ocean Pycnocline. Ann. Rev. Mar. Sci. **14**: 405–430. doi:10.1146/annurev-marine-010419-011012
Olsen, A., R. M. Key, S. Van Heuven, and others. 2016. The global ocean data analysis project version 2 (GLODAPv2) - An internally consistent data product for the world ocean. Earth Syst. Sci. Data **8**: 297–323. doi:10.5194/essd-8-297-2016
Portela, E., N. Kolodziejczyk, C. Maes, and V. Thierry. 2020. Interior Water-Mass Variability in the Southern Hemisphere Oceans during the Last Decade. J. Phys. Oceanogr. **50**: 361–381. doi:10.1175/JPO-D-19-0128.1
Primeau, F. W., M. Holzer, and T. DeVries. 2013. Southern Ocean nutrient trapping and the efficiency of the biological pump. J. Geophys. Res. Ocean. **118**: 2547–2564. doi:10.1002/jgrc.20181
Qu, T., S. Gao, and R. A. Fine. 2020. Variability of the Sub-Antarctic Mode Water Subduction Rate During the Argo Period. Geophys. Res. Lett. **47**. doi:10.1029/2020GL088248
Le Quéré, C., R. M. Andrew, P. Friedlingstein, and others. 2018. Global Carbon Budget 2018. Earth Syst. Sci. Data **10**: 2141–2194. doi:10.5194/essd-10-2141-2018
Raphael, M. N. 2004. A zonal wave 3 index for the Southern Hemisphere. Geophys. Res. Lett. **31**: 1–4. doi:10.1029/2004GL020365
Rintoul, S. R., and M. H. England. 2002. Ekman transport dominates local air-sea fluxes in

driving variability of subantarctic mode water. J. Phys. Oceanogr. **32**: 1308–1321. doi:10.1175/1520-0485(2002)032<1308:ETDLAS>2.0.CO;2

Rödenbeck, C., R. F. Keeling, D. C. E. Bakker, and others. 2013. Global surface-ocean pCO2 and sea-Air CO2 flux variability from an observation-driven ocean mixed-layer scheme. Ocean Sci. **9**: 193–216. doi:10.5194/os-9-193-2013

Roemmich, D., and J. Gilson. 2009. The 2004-2008 mean and annual cycle of temperature, salinity, and steric height in the global ocean from the Argo Program. Prog. Oceanogr. **82**: 81–100. doi:10.1016/j.pocean.2009.03.004

Russell, J. L., and A. G. Dickson. 2003. Variability in oxygen and nutrients in South Pacific Antarctic Intermediate Water. Global Biogeochem. Cycles **17**: n/a-n/a. doi:10.1029/2000GB001317

Sabine, C. L., R. A. Feely, N. Gruber, and others. 2004. The Oceanic Sink for Anthropogenic CO 2. Science (80-.). **305**: 367–371.

Sabine, C. L., and T. Tanhua. 2010. Estimation of Anthropogenic CO $_2$ Inventories in the Ocean. Ann. Rev. Mar. Sci. **2**: 175–198. doi:10.1146/annurev-marine-120308-080947

Sallée, J. B., K. G. Speer, and S. R. Rintoul. 2010. Zonally asymmetric response of the Southern Ocean mixed-layer depth to the Southern Annular Mode. Nat. Geosci. **3**: 273–279. doi:10.1038/ngeo812

Sarmiento, J. L., N. Gruber, M. A. Brzezinski, and J. P. Dunne. 2004. High-latitude controls of thermocline nutrients and low latitude biological productivity. Nature **427**: 56–60. doi:10.1038/nature10605

Sloyan, B. M., and S. R. Rintoul. 2001. The Southern Ocean Limb of the Global Deep Overturning Circulation*. J. Phys. Oceanogr. **31**: 143–173. doi:10.1175/1520-0485(2001)031<0143:TSOLOT>2.0.CO;2

Speer, K., S. R. Rintoul, and B. Sloyan. 2000. The Diabatic Deacon Cell*. J. Phys. Oceanogr. **30**: 3212–3222. doi:10.1175/1520-0485(2000)030<3212:TDDC>2.0.CO;2

Sutton, A. J., N. L. Williams, and B. Tilbrook. 2021. Constraining Southern Ocean CO2 Flux Uncertainty Using Uncrewed Surface Vehicle Observations. Geophys. Res. Lett. **48**: 1–9. doi:10.1029/2020GL091748

Tamsitt, V., I. Cerovečki, S. A. Josey, S. T. Gille, and E. Schulz. 2020. Mooring Observations of Air–Sea Heat Fluxes in Two Subantarctic Mode Water Formation Regions. J. Clim. **33**: 2757–2777. doi:10.1175/JCLI-D-19-0653.1

Verdy, A., S. Dutkiewicz, M. J. Follows, J. Marshall, and A. Czaja. 2007. Carbon dioxide and oxygen fluxes in the Southern Ocean: Mechanisms of interannual variability. Global Biogeochem. Cycles **21**: 1–10. doi:10.1029/2006GB002916

Verdy, A., and M. R. Mazloff. 2017. A data assimilating model for estimating Southern Ocean biogeochemistry. J. Geophical Res. Ocean. **122**: 1–22. doi:10.1002/2016JC012650

Williams, N. L., L. W. Juranek, R. A. Feely, and others. 2017. Calculating surface ocean pCO2 from biogeochemical Argo floats equipped with pH: An uncertainty analysis. Global Biogeochem. Cycles **31**: 591–604. doi:10.1002/2016GB005541

Williams, N. L., L. W. Juranek, R. A. Feely, and others. 2018. Assessment of the carbonate chemistry seasonal cycles in the Southern Ocean from persistent observational platforms. J. Geophys. Res. Ocean. **123**: 1–20. doi:10.1029/2017JC012917

Wolf, M. K., R. C. Hamme, D. Gilbert, I. Yashayaev, and V. Thierry. 2018. Oxygen Saturation Surrounding Deep Water Formation Events in the Labrador Sea From Argo-O 2 Data. Global Biogeochem. Cycles **32**: 635–653. doi:10.1002/2017GB005829

982 Wong, A. P. S., N. L. Bindoff, and J. A. Church. 1999. Large-scale freshening of intermediate
983 waters in the Pacific and Indian oceans. Nature **400**: 440–443. doi:10.1038/22733
984 Wu, Y., D. C. E. Bakker, E. P. Achterberg, and others. 2022. Integrated analysis of carbon
985 dioxide and oxygen concentrations as a quality control of ocean float data. Commun. Earth
986 Environ. **3**: 92. doi:10.1038/s43247-022-00421-w
987 Zeebe, R. E., and D. A. Wolf-Gladrow. 2001. CO2 in Seawater: Equilibrium, Kinetics, Isotopes,
988 Elsevier.
989